Manuscript 15 December 2020/PSt

Manuscript submitted for publishing in AGU Journal Space Weather

Transpolar convection and magnetospheric ring current relations: real time applications of the Polar Cap (PC) indices.

Peter Stauning
Danish Meteorological Institute, Copenhagen, Denmark
Mail: pst@dmi.dk

Abstract. The relations between transpolar plasma convection intensities recorded by the Polar Cap (PC) indices and magnetospheric ring current intensities recorded by the asymmetric ASY-H indices and the symmetric Dst and SYM-H indices are examined. The present work believed to be the first of its kind examines the validity of previously derived relations between polar cap and ring current indices when used in real time applications. Polar cap (PC) indices are here derived in simulated real-time versions by using past data only from -40 days up to current time in the construction of the quiet reference levels (QDCs) for the magnetic data. From analyses spanning a decade (2009-2018), equivalent ASY-H index values were derived from a linear relation with simulated real-time PCN (North) and PCS (South) indices combined to form the non-negative PCC indices. For cases of strong magnetic storms (Dst(peak)<-100 nT, the equivalent ASY-H indices were found to agree well with reported (real) ASY-H index values. The simulated real-time PCC indices, furthermore, have been used in a PC-based source function to derive equivalent values of the total ring current indices Dst (or SYM-H) up to one hour ahead of time. With integration of the source function throughout a decade (2009-2018) with no attachment to reported Dst values, the simulated real-time equivalent Dst indices displayed close agreement with real Dst index values. The applied method could be used without modifications to generate PC index values and derived ASY-H and Dst (or SYM-H) index values in real-time space weather applications..

1. Introduction.

The hourly Dst index (Sugiura and Kamei, 1981) and the equivalent 1-min SYM-H index values derived from low-latitude magnetic observations are considered to represents the intensity of the magnetospheric ring current of mirroring ions drifting near equator at distances of 4 to 6 Earth Radii (R_E). A relation between the accumulated kinetic energy of the charged particles encircling the Earth and the Dst* indices (i.e., the Dst indices corrected for magnetopause current effects) is provided by the Dessler-Parker-Sckopke relation (Dessler and Parker, 1959; Sckopke, 1966). The ring currents are believed to result from solar wind-magnetosphere interactions. Thus, building the ring currents could be considered to represent the input of energy from the solar wind conveyed by the electric fields extended over the magnetosphere (Burton et al., 1975).

In addition to building the ring currents, the incoming solar wind energy is also used to power further disturbance processes such as polar and auroral magnetic substorm activity that may generate upper atmosphere heating and strong auroral currents which, in turn, may generate geomagnetically induced currents (GIC) in conducting structures on ground. The strongest GIC cases could seriously disturb power grids (Kappenman, 2010; Pulkkinen et al., 2017; Stauning, 2013, 2020a).

Thus, monitoring the energy input from the solar wind to the magnetosphere has strong relevance for operational space weather-related applications. In addition, investigations of the relations between ring current intensities and other solar wind and related geospace parameters may help understanding and modelling the ring currents and enlighten their association with polar cap plasma convection processes. Both phenomena are essential parts of the structure and dynamics of the magnetosphere in relation to its interaction with the solar wind.

The standard polar cap PCN (North) indices are based on magnetic observations at Qaanaaq (THL) in the northern polar cap, while PCS (South) index values are based on magnetic observations at Vostok in Antarctica. The PC indices are derived from the magnetic variations generated by the transpolar convection of plasma and magnetic fields and scaled to level the Kan and Lee (1979) merging electric field, E_M, in the solar wind (Troshichev et al., 1988). In consequence of their close relations to E_M, the PC indices are considered to represent the input of energy from the solar wind.

Thus, one might expect close relations between the ring current intensities, scaled by the partial (asymmetric) and the total (symmetric) 1-min indices ASY-H and SYM-H or the hourly Dst indices, and the polar cap indices, PCN and PCS. With the two available polar cap indices the question arises which one or which combination of the two PC indices is the most representative version. Furthermore, there is also the conceptual problem that the individual (hemispherical) PC indices and also their averages may take large negative values at times without causing the ring current to reverse its direction of revolution, but mostly just causing weakening of its strength.

An effective solution to both problems was found by the introduction of the non-negative polar cap PCC index combination (Stauning, 2007). The PCC indices are derived as the average of positive values of the two hemispherical polar cap PC indices disregarding (zero filling) negative values. It has been demonstrated that the PCC indices have a higher degree of correlation with the merging electric fields than either of the individual polar cap indices or their averages (Stauning et al., 2008; Stauning, 2012, 2020c).

Basic models of the magnetospheric convection of plasma and embedded magnetic fields are based on the two-cell convection system (DP2) introduced by Dungey (1961). The cross-polar cap electric fields that generate the transpolar plasma flow are linked to region 1 currents generated at the magnetospheric boundary regions while the lower-latitude return flows are driven by electric fields linked to region 2 currents extending from the auroral regions to the ring current regime. In the DP2 system the magnetospheric tail region is loaded by plasma and embedded magnetic fields convected over the polar caps from the front to the rear of the magnetosphere. Enhanced plasma pressure and occasional substorm activity in the tail region may cause injection of energetic plasma from the tail to the partial ring current regime at the rear of the ring current region.

Such processes may cause enhancements of the asymmetric (partial) ring currents which are related directly to the transpolar convection and contribute to the building of the symmetric (total) ring currents. The gradual building of the total ring current intensities could be estimated by integration of a PC index-based source function. Both the asymmetrical (partial) ring currents scaled by ASY-H indices and symmetrical (total) ring current intensities scaled by Dst or SYM-H involve geomagnetic activity at both polar caps conveniently scaled by the PCC indices.

The relations between PC indices and the ring current ASY-H and Dst (or SYM-H) indices have been investigated previously by Stauning et al. (2008), Stauning (2012), and in a recent work by Stauning (2020c). The target in the present work is to examine the validity of the established relations based on post-event data for use in real-time applications. Thus, the PC indices are derived here in simulated real time versions by using past data only with respect to current time in the construction of the undisturbed reference levels named the quiet day curve (QDC). The QDCs are

needed for calculation of the magnetic variations that are subsequently processed with tabulated scaling parameters for deriving PC index values. In real-time applications where the geomagnetic data are currently available, this approach would provide actual ring current intensity values including the actual ASY-H index and gradient values for the Dst (or SYM-H) indices enabling estimates of their values up to one hour ahead.

2. The Polar Cap indices, PCN, PCS, and PCC.

The magnetic variations providing the basis for the polar cap indices are related to the transpolar convection of plasma and embedded magnetic fields driven by the interaction of the solar wind with the Earth's magnetosphere. The interaction is controlled by the solar wind merging (or "geo-effective") electric fields, E_M, defined by Eq. (1) from the solar wind velocity, V_{SW}, and the components B_Y and B_Z of the interplanetary magnetic field (IMF) in its Geocentric Solar Magnetosphere (GSM) representation (Kan and Lee, 1979):

$$E_M = V_{SW} \cdot (B_Y^2 + B_Z^2)^{½} \cdot \sin^2(\theta/2) \; : \; \theta = \arctan(B_Y/B_Z) \quad (1)$$

The magnetic variation vectors, $\Delta\mathbf{F}$, when projected to an optimum direction considered to be perpendicular to the dominant forward transpolar convection direction, are assumed to be related to the merging electric fields by:

$$\Delta F_{PROJ} = \alpha \cdot E_M + \beta \quad (2)$$

where the scaling parameters, slope (α) and intercept (β), are defined from an epoch of past data by the regression defined in Eq. 2.

Thus, to level with E_M, the PC index is defined by Eq. 3:

$$PC = (\Delta F_{PROJ} - \beta)/\alpha \approx E_M \quad (3)$$

The optimum direction is characterized by its angle (φ) to the polar cap dawn-dusk meridian. The angle is found by seeking maximum correlation between the projected magnetic variations and the non-negative merging electric field values. This process also determines the delay from the position where the solar wind parameters are measured to the observatory position in the polar cap where the effects are recorded. A detailed description of the derivation methods may be found in Stauning et al. (2006) or Stauning (2016).

It is important to realize that the transpolar convection has two basic modes, forward and reverse convection patterns. The forward (day to night) transpolar convection is part of the DP2 two-cell convection patterns with return flows in the auroral regions. DP2 patterns are observed during conditions where IMF is either southward (negative) or just weak. The reverse convection mode is part of the DP3 two-cell convection patterns observed during strong northward (positive) IMF conditions. The two modes, DP2 and DP3, have very different relations to solar wind properties and geospace disturbances. Usually, the DP2 forward convection mode have much wider latitudinal and longitudinal patterns and much stronger effects on geomagnetic storm and substorm conditions than the DP3 reverse convection mode.

The estimate of optimum direction angle is mostly based on DP2 (forward) convection samples since they are more frequent than the DP3 conditions. Furthermore, the merging electric field values are generally small for northward IMF (NBZ) conditions reducing their effects on the correlation results. Thus, the forward convection conditions generate positive values of the projected magnetic variations and mostly positive values of the derived PC indices since α in Eq. 3 is positive and β small while the reverse convection conditions, correspondingly, generate negative PC index values.

In the present ”DMI2016” PCN and PCS versions (Stauning, 2016), the reverse convection cases are omitted in the regression of Eq. 2 used to derive the scaling parameters. In the past, the PCN version developed by Vennerstrøm (1991) and the PCN and PCS versions issued by the Arctic and Antarctic Research Institute (AARI), named AARI#1, AARI#2, AARI#3, AARI#4, and AARI#5 and also the version here named IAGA2014 (Matzka, 2014; Nielsen and Willer, 2019) include forward as well as reverse convection samples in the regression (Eq. 2) mixing DP2 and DP3 conditions with the adverse consequences discussed in Stauning (2015, 2018b). The IAGA2014 version was endorsed by the International Association for Geomagnetism and Aeronomy (IAGA) by its resolution no. 3 (2013).

The PCC indices defined in Stauning (2007) are derived by combining non-negative values of the PCN and PCS indices as shown in Eq. 4:

PCC = (PCN if >0 or else 0 + PCS if >0 or else 0) /2. (4)

Thus, the PCC indices represent the mean level of forward convection (DP2) intensities in the two polar caps taken as an entity.

3. Deriving PC indices in real time.

The present IAGA-recommended near-real time PC index versions are not considered reliable as explained in Stauning (2018a, 2020b). Their derivation procedures are not publicly available. Their scaling parameters are based on samples from a mix of DP2 and DP3 conditions. Based on the approach defined in Janzhura and Troshichev (2011), the reference level calculations comprises a cubic spline-based extrapolation procedure to define the IMF B_Y-related “solar wind sector” terms, H_{SS} and D_{SS} to be added to the slowly varying (30-days) QDCs for the two components. The cubic spline-based SS-terms in the reference level generate excessive excursions reaching magnetic storm level at frequently occurring (not necessarily extreme) variations in the IMF B_Y conditions or by short interruptions of the data supply. Moreover, these near-real time indices, which have been issued since February 2014, have never been verified or applied to published works.

In a different approach using Solar Rotation Weighted (SRW) QDC techniques (Stauning, 2011) in the calculations, the post-event reference levels are estimated from weighted averages of the quietest samples collected at comparable conditions within ±40 days of the day of interest. In the simulated real-time approach (SRT), the quiet samples are collected from the past -40 days only. With previously defined (tabulated) calibration parameters (φ, α, β) and access to polar magnetic data in real-time, it is now possible to calculate PC index values in real time with good precision and high reliability.

Examples of the QDC reference levels (with secularly varying base levels subtracted) for Vostok throughout 2015 are displayed in Figs. 1a,b and 2a,b. Figures (a) display the X-components while figures (b) display the Y-components. Fig. 1 displays the full SRW QDC values (±40 days) while Fig. 2 displays the simulated real-time HSRW (half solar rotation) QDC values (-40 days).

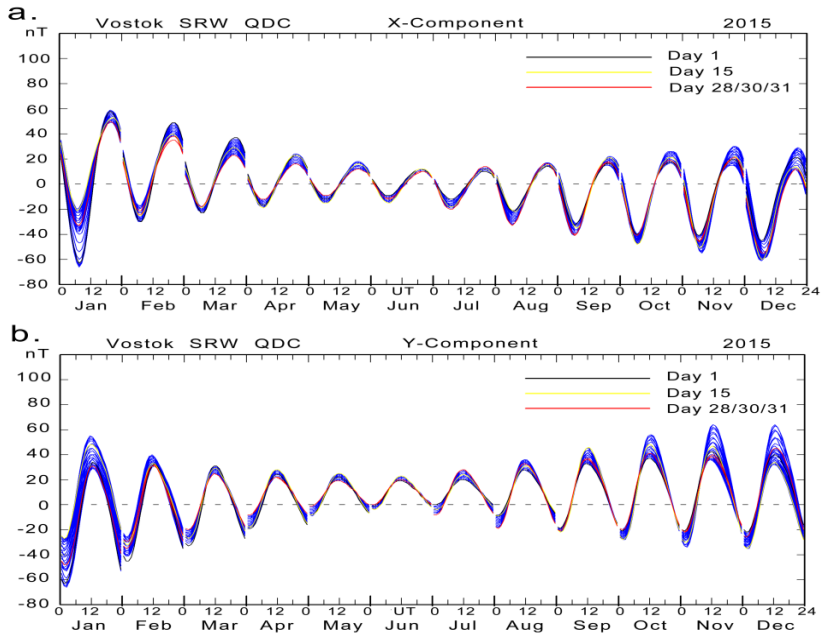

Fig. 1. Vostok QDC reference levels 2015 by SRW method. (a) X-component (b) Y-component.

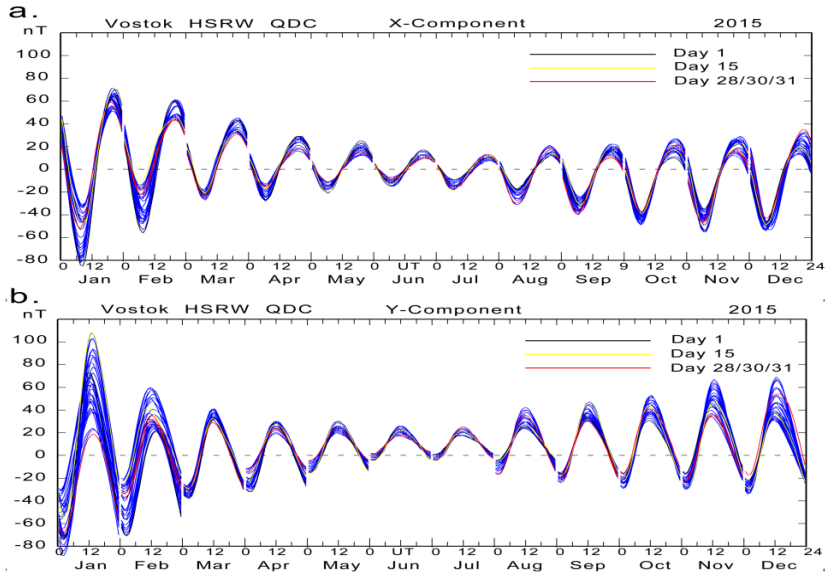

Fig. 2. Vostok QDC reference levels 2015 by HSRW method. (a) X-component (b) Y-component.

In these diagrams there is a QDC curve for each day of the year. The daily QDC curves are drawn on top of each other in blue line. For day 1 (in black line), day 15 (yellow), and for the last day of the month (in red line) the QDCs are re-drawn on top of the other QDCs. Going from the black curves through the yellow ones to the red curves provides an impression of the development of the QDCs throughout the month. The QDCs derived this way may also accommodate moderate secular variations in the magnetometer base levels as illustrated by the slight sloping of the assembly of curves in Figs. 1 and 2. For most months the differences between the post-event and simulated real-time QDCs are less than 10 nT in each component which correspond to differences in PC index values of less than 0.5 mV/m.

4. Relations of PCN, PCS and PCC to the merging electric field.

It was demonstrated in Stauning (2007) at the presentation of the PCC index concept that the PCC indices had a higher degree of correlation with the merging electric fields, E_M, than either of the individual, PCN or PCS, indices. This feature was confirmed in Stauning et al. (2008) and Stauning (2012). In a recent investigation (Stauning, 2020c) the comparison of correlation results was extended to comprise also the plain average, PCA, of PCN and PCS as well as selections of either local winter or summer PC index values (PCW, PCU). Furthermore, the correlation of E_M with a PCS index (PCD) based on using magnetic data from Dome-C observatory (Chambodut et al., 2009; Di Mauro, 2014) has been examined. A comparison of the correlations between E_M and PCC, PCN, and PCS values throughout 2009 to 2018 is presented in Fig. 3a here (see Stauning, 2020c). In this figure, the PC indices are based on post-event derivation. The corresponding correlation coefficients derived from simulated real-time PC indices throughout 2009 to 2018 are displayed in Fig. 3b.

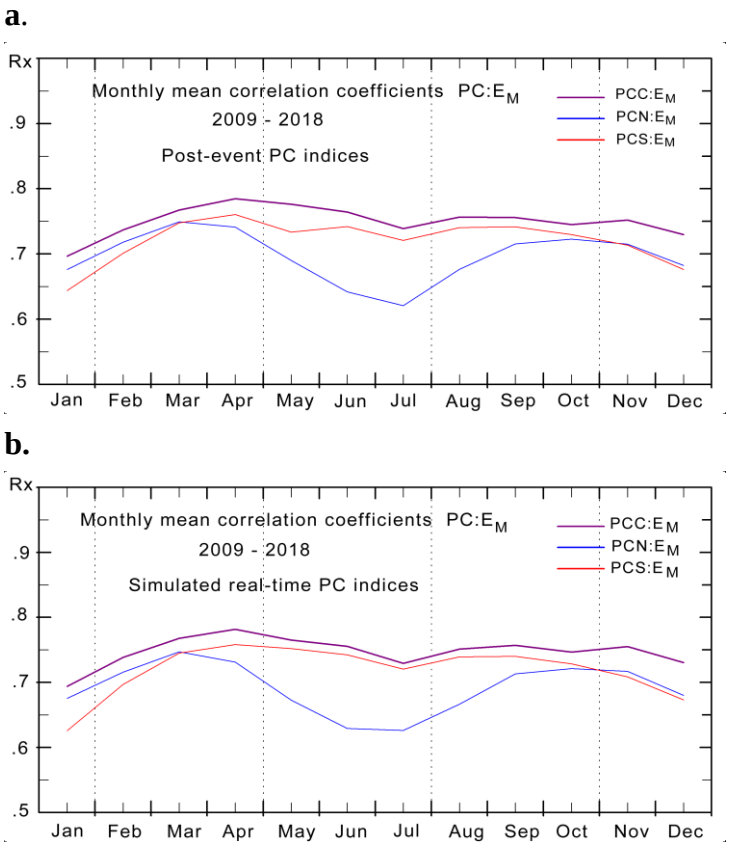

Fig. 3. Display of monthly average coefficients for the correlation between E_M and PCN (blue line), PCS (red), and PCC (magenta). (a) Post-event PC indices 2009-2018 (similar to Fig. 6 of Stauning, 2020c). (b) Simulated real time PC indices 2009-2018.

A summary of epoch-average correlation coefficients for the relations between E_M and the various index types in their post-event (PE) and simulated real time (SRT) versions is presented in Table 1. It is seen by comparing Fig. 3a to 3b, like also noted in Table 1, that the real-time PC indices display almost the same correlations with E_M as those found for the post-event values. It is also evident from Figs. 3a, b and Table 1 that the correlation between E_M and PCC or PCCD (PCC using PCD for poor PCS values) is superior to the correlation coefficients obtained with PCN or PCS and

also display much less seasonal variation. Thus, applications used to estimate values of the solar wind merging electric field whether in real-time or post-event situations could take advantage by using the PCC (PCCD) index version.

Table 1. Correlation coefficients for relations between E_M and various PC index versions.

Epoch 2009-2018	PCCD	PCC	PCN	PCS	PCD
Post-Event	**0.753**	0.751	0.696	0.722	0.736
Real-Time	**0.749**	0.748	0.692	0.720	0.728

It might be noted that the PCS indices (here named PCD) based on using data from Dome-C magnetometer provide slightly better correlations with E_M than PCS indices based on data from the standard PC observatory, Vostok, whether in post-event or real-time versions. Another observation is the lower correlations of PCN with E_M than seen for either of the PCS indices.

5. The PC indices and the asymmetrical ring current index, ASY-H.

The asymmetrical (partial) ring current indices, ASY-H, are provided by Kyoto WDC-C2 (Iyemori et al., 2000) as 1-min values. For the present statistical study a less detailed time resolution is considered appropriate. Hence, the ASY-H and the polar cap PCN and PCS indices, have been averaged to form 15-min samples. For the series of indices, the 15-min averaging intervals for the ASY-H indices were shifted with respect to the corresponding intervals for the PC indices to obtain maximum correlation.

The present investigation has considered 4-days intervals of major geomagnetic storms with Dst(peak)<-100 nT occurring between 2009 and 2018 and with the onset occurring on the first day. A complete list of these geomagnetic storm events, times and amplitudes of their peak intensities (minimum hourly Dst or 15-min SYM-H values) are provided in the Appendix. These values are supplemented by corresponding times and max amplitudes for the PCC indices throughout each storm interval.

Figs. 4a and 4b display scatter plots of 15-min ASY-H index values against PCC values derived by post-event (PE) or by simulated real-time (SRT) calculations, respectively. The 8 min delay noted in the figure was found to provide least RMS deviation and optimum correlation for samples of the two index series.

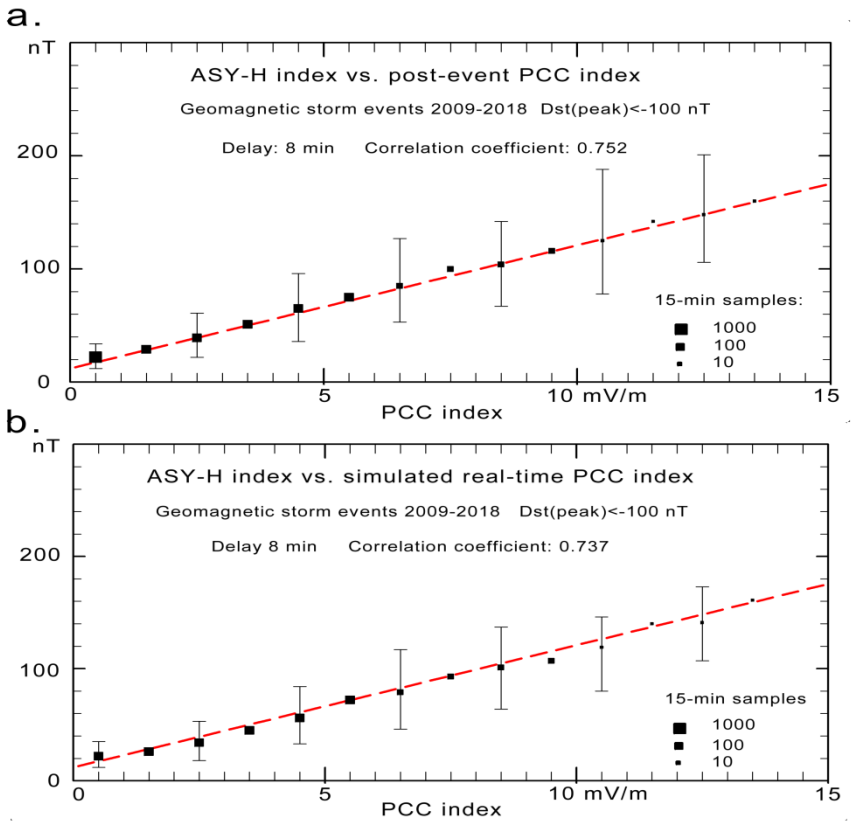

Fig. 4. (a) Scatter plot of ASY-H against post-event PCC index values for storm events in 2009-2018. The black squares indicate average values and number of 15-min samples within each unit interval in PCC, while the error bars at every other unit interval indicate standard deviation (spread). The red dashed line in Fig.4a is based on the regression in Stauning (2020c). (b.) Corresponding scatter plot of ASY-H against simulated real-time PCC index values for storm events 2009-2018. The red line is repeated from Fig 4a.

A linear relation between 15-min samples corresponding to the dashed line in Fig. 4a was estimated by least squares regression analyses based on data from storm events 1992-2018 to provide the relation expressed in Eq. 5 (from Stauning, 2020c):

$$\text{ASY-H}_{EQ} = 10.9 \cdot \text{PCC} + 16. \quad [\text{nT}] \qquad (5)$$

The results from comparing the reported (real) ASY-H values with equivalent ASY-H_{EQ} index values provided by Eq. 5 from using the post event (PE) or simulated real-time (SRT) PCC index values are summarized in Table 2.

Table 2. Summary of post-event and real-time ASY-H calculations. Magnetic storms 2009-2018.

PCC version	No. samples	Mean ASY-H	Mean PCC	Mean Error	RMS error	Correlation
Post-Event	7349	38.5 nT	2.07 mV/m	5.9 nT	21.7 nT	0.752
Real-Time	7350	38.5 nT	2.46 mV/m	1.8 nT	21.6 nT	0.737

Further details of the relations between the ASY-H indices and the PCC indices as well as the individual PCN and PCS indices and further possible combinations may be found in Figs. 9, 10 and Tables 2 and 5 of Stauning (2020c). It might be noted that the correlation coefficient for the ASY-H

and PCC index relation is considerably higher that the corresponding coefficients for relation between ASY-H and PCN, PCS, and PCA, the average of PCN and PCS (see Table 4 in section 10). In addition, using the non-negative PCC index resolves the conceptual dilemma in handling the frequently occurring cases of negative PCN or PCS values since the ASY-H indices rise for increasing positive as well as increasing negative PCN or PCS index values making the relations ambiguous (see Figs. 10a-c of Stauning, 2020c).

6. The PC indices and the symmetrical ring current index, SYM-H.

The relations between post-event (PE) or simulated real-time (SRT) PCC indices and SYM-H index values corresponding to those displayed in Figs. 4a,b for the ASY-H indices are presented in Figs. 5a,b. For the SYM-H vs. PCC relations, contrary to the ASY-H vs. PCC relations, it was not possible to define the delay within examined 4 hours that would provide maximum correlation. Table 3 presents imposed delays (SYM-H after PCC) and derived correlation coefficients for the 4-days magnetic storm events (Dst<-100 nT) with onset on the first day established throughout 2009-2018. The implications of the results are discussed in section 9.

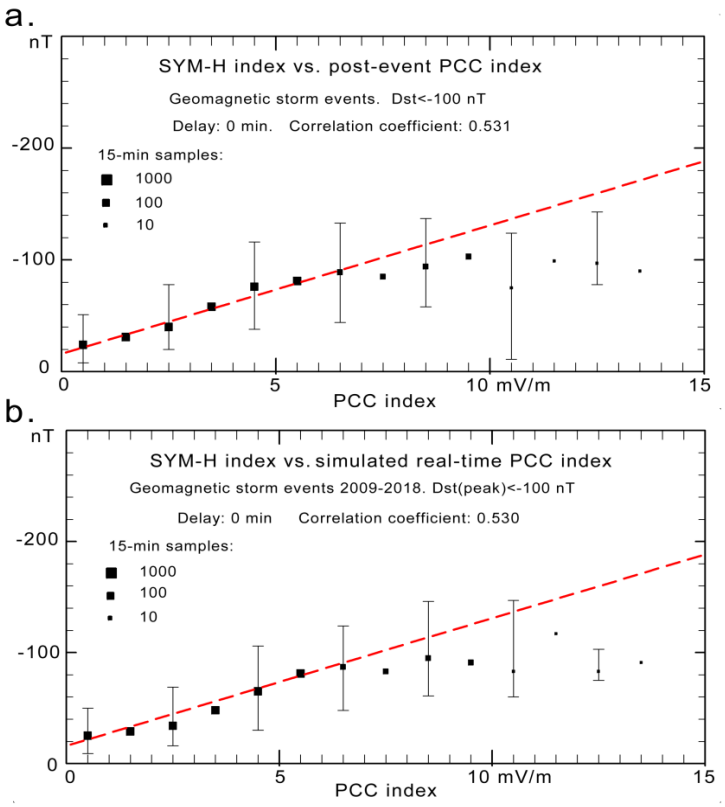

Fig. 5. (a) Scatter plot of SYM-H against post-event PCC index values for storm events in 2009-2018. The black squares indicate average values and number of 15-min samples within each unit interval in PCC, while the error bars at every other unit interval indicate standard deviation. The red dashed lines are drawn for illustration only. (b.) Corresponding scatter plot of SYM-H against simulated real-time PCC index values using the same red dashed line.

Table 3. SYM-H vs. PCC correlation coefficients during major magnetic storms at various delays.

PCC version	0 min.	60 min	120 min	180 min	240 min
Post-event	0.531	0.619	0.632	0.636	0.643
Real-time	0.530	0.614	0.625	0.628	0.632

The differences between the SYM-H vs. PCC displays in Fig. 5a for the post-event PCC version and in Fig. 5b for the simulated real-time version are hardly discernible. The differences in correlation coefficients depicted in Table 3 are also quite small.

7. Examples of displays of ASY-H and SYM-H during magnetic storms.

In view of the good correlation between ASY-H and PCC demonstrated in Figs. 4a,b and Table 2 (Rx(PE)=0.752, Rx(SRT)=0.737) for a delay of 8 min and the fair correlation between SYM-H and PCC shown in Figs. 5a,b and Table 3 (Rx(PE)=0.619, Rx(SRT)=0.614) for a delay of 60 min, it might be expected that displays of the indices would show a fair degree of similarity with the PCC-based equivalent index values.

The slopes, ASY-H/PCC=10.9 [nT/(mV/m)] and SYM-H/PCC=-11.5 [nT/(mV/m)], defined from the processing of 98 storm event (Stauning, 2020c), have been used here with the simulated real-time PCC values to derive equivalent ASY-H_{EQ} and SYM-H_{EQ} values for selected magnetic storm events among those used to derive the relations. Examples for the 4-days magnetic storms on 16-19 March and 22-25 June 2015 are displayed in Figs. 6a,b using the simulated real-time PCC versions. Whether using post-event or real-time PCC index values changes little in the displays

.

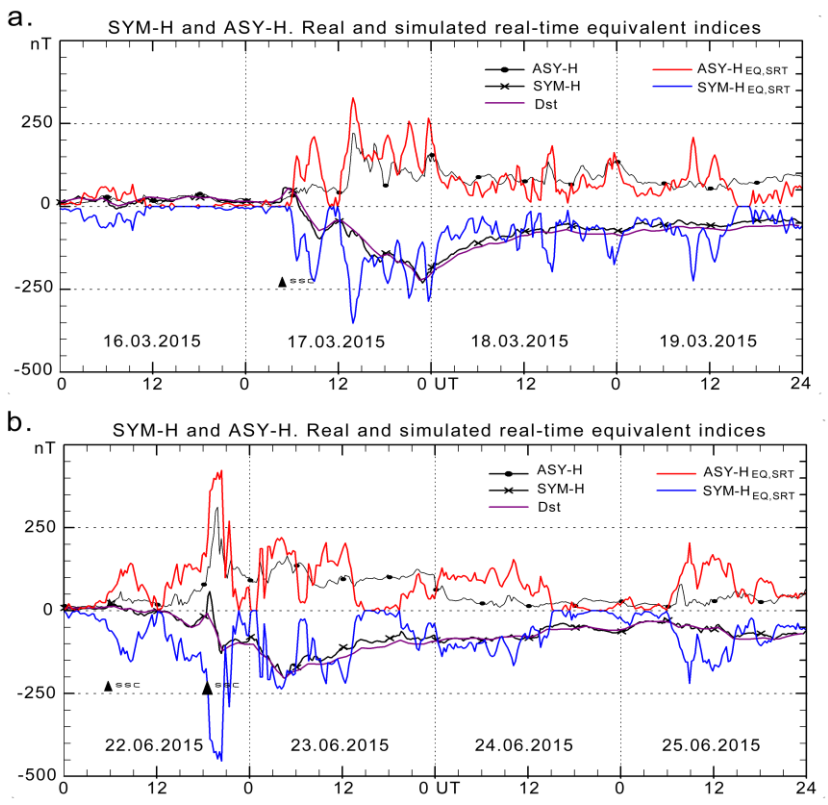

Fig. 6 Magnetic storms (a) 16-19 March 2015, (b) 22-25 June 2015. The upper fields display real ASY-H indices (black line with dots) and equivalent ASY-H_{EQ} values (red) converted from PCC index values by scaling. The lower fields display real SYM-H (black line with crosses) and Dst indices (magenta line), and equivalent SYM-H_{EQ} index values (blue) converted from PCC by scaling.

Note in Figs. 6a and 6b the coarse agreement between SYM-H or ASYM-H and their PCC-based equivalent index series. However, the detailed courses of the ring current indices are rather different from those of the PCC-based equivalent versions. The best agreement is seen in the displays of the ASY-H indices in the upper fields while PCC-based SYM-H variations with periods of a few hours are hardly noticeable at all in the real SYM-H or Dst indices. Like indicated by the lack of a delay providing maximum correlation demonstrated in Table 3, the direct correlation of PC index values with SYM-H or Dst indices is not meaningful. Looking for rules connecting peak times and amplitudes of PC and SYM-H or Dst indices like those expressed in Troshichev et al. (2011a), Troshichev and Janzhura (2012), Troshichev (2017), Troshichev and Sormakov (2018), or in ISO/TR23989:2020 appears pointless.

8. PC indices in a source function for the total ring current indices, SYM-H and Dst.

8.1 The relation of post-event PC indices to ring current indices.

The approach suggested in Stauning et al. (2008) and further developed in Stauning (2012, 2020c) has been applied to provide extended examinations of the relations between real-time PC indices and the 1-h Dst and 1-min SYM-H indices. Thus, the PCC indices are used in a source function to describe the gradient in the Dst indices rather than in correlations with the actual ring current index values. Following Burton et al. (1975) the change in the Dst index with time could be written:

$$dDst^*/dt\ [nT/h] = Q[nT/h] - Dst^*\ [nT] / \tau\ [h] \qquad (6)$$

where Dst* is the recorded Dst index values corrected for contributions from magnetopause currents (MPC) related mostly to the solar wind dynamic pressure. The quantity Q (in nT/h) is the source term while the last term in Eq. 6 is the ring current loss function controlled by the decay time constant, τ, here measured in hours. For the small actual MPC corrections, the Dst dependent statistical values provided in Jorgensen et al. (2004) have been used here. The decay function in the version provided by Feldstein et al. (1984) uses τ = 5.2 h for large disturbances where Dst < -55 nT, and τ = 8.2 h for small disturbances where Dst >-55 nT. Now, the relation in Eq. 6 may provide derived Dst index values by integration from known start conditions, once the source term is defined.

From the investigations in Stauning (2020c), the source term was defined to become Q(nT/h) = -4.5 (nT/h)/(mV/m)·PCC(mV/m) in order to provide the best agreement between real and equivalent Dst values for an integration starting from Dst=0 on 1 January 1992 and proceeding to 31 December 2018 without attachment to the real Dst values. From the same process, the decay time constants were redefined to become τ = 5.5 h for large disturbances where Dst < -52 nT, and τ = 7.0 h for small disturbances where Dst >-52 nT. The compensation for PC saturation effects was accomplished by adjustment of PCC amplitude by adding a linearly rising amount to PCC values in excess of 5 mV/m:

$$PCCeff=PCC \text{ for } PCC<5 \text{ mV/m. : } PCCeff=PCC+0.60\cdot(PCC-5) \text{ for } PCC>5 \text{ mV/m} \qquad (7)$$

The overall correlation coefficient for the relation between Dst and the equivalent Dst values was 0.856, the mean difference was -0.01 nT while the RMS difference was 12.3 nT (Stauning, 2020c). The relations from Stauning (2020c) derived by using post-event PC index values shall be applied here using simulated real-time PC indices to replace post-event PC index values in the source function.

8.2. Simulated real-time derivation of ring current intensities from PC-based source functions during magnetic storm events.

The updated parameters and simulated real-time PC index values were used for integration of the source function in Eq. 6 to give simulated real-time equivalent ring current index values where $Dst_{EQ,SRT}$ would be the hourly average of 1-min SYM-$H_{EQ,SRT}$ values. Examples are presented in Figs. 7a,b where the integration of the source function has started at the real Dst values recorded at the start of the intervals and then allowed to proceed independently throughout the 4 days in each set. This type of processing was used in Stauning (2020c) with post-event PCC values. Here we apply the simulated real-time PCC indices.

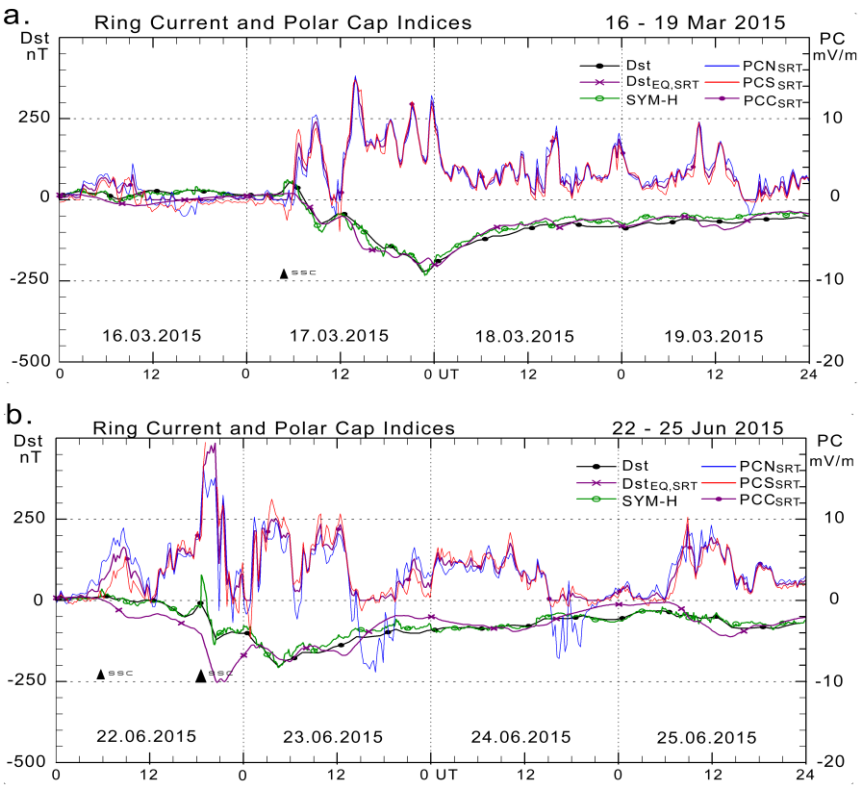

Fig. 7. Examples of real Dst (black line, dots) and SYM-H (green, open dots) values, and simulated real-time equivalent $Dst_{SRT,EQ}$ (magenta, crosses) values calculated from the PCC-based source function by using simulated real-time values of the PC indices. Values of PCC_{SRT} (magenta), PCN_{SRT} (blue), and PCS_{SRT} (red) are displayed in the upper fields on the right scale. (a) 16-19 March 2015. (b) 22-25 June 2015.

The data basis for Fig. 7 comprises the events displayed in Fig. 6. The SYM-H values (green line) track the Dst values quite well except for variations in response to the Storm Sudden Commencements (SSC). The SSC events are included in the figures with markings of their times of occurrence and amplitudes by the upward pointing peaks and the sizes of the triangular symbols.

The correlation between Dst and the simulated real-time (equivalent) Dst values is Rx=0.960 for Fig. 2a, which is better than the average correlation coefficient for the events of epoch 2009-2018 of 0.821 (cf. Table A1 of the Appendix). For Fig. 2b the correlation coefficient is Rx=0.775 making it the worst example in 2015 (Table A1).
Compared to the initial (post-event) version in Stauning (2020c), the use of simulated real-time PC indices has generated very little change in correlation coefficients and other parameters resulting from the calculations such as the mean and rms differences between real and equivalent Dst values.

The reduced range for the QDC derivation from the post-event standard range of ±40 days to just -40 days up to actual time has little effect on the reference levels for the PC indices. Furthermore, contrary to the IAGA-recommended cubic spline-based extrapolation method (see Stauning, 2018a), the QDC values are not strongly dependent on singular values or missing samples and generate reliable reference levels and index values.

Diagrams corresponding to Figs. 7a and b and a summary table of Dst and SYM-H peak values are provided in Table A1 of the Appendix for all 20 cases of strong magnetic storms with Dst<-100 nT occurring during the decade from 2009 to 2018. For these 20 storm events with peak amplitudes ranging from Dst=-100 to -222 nT, the differences between the Dst values and the simulated real-time equivalent Dst could be characterized by the average correlation coefficient, Rx=0.821 (0.824), the mean absolute difference, Dif(abs)=19.3 nT (19.7 nT), and the average rms difference, Dif(rms)=24.3 nT (24.7 nT). The numbers in parentheses are the corresponding figures for the relations based on post-event PCC index values derived with full SRW (±40 days) estimation of the QDCs. The small magnitudes of the differences demonstrate that the real-time estimates of Dst are as valid as the post-event estimates.

8.3. Extended simulated real-time derivation of ring current intensities

In a further development of the PC-based source function concept, the equivalent simulated real-time Dst indices have been derived for the decadal interval from 2009 to 2018 without attachment to the real Dst index. The interim results for 2015 are displayed in Fig. 8.

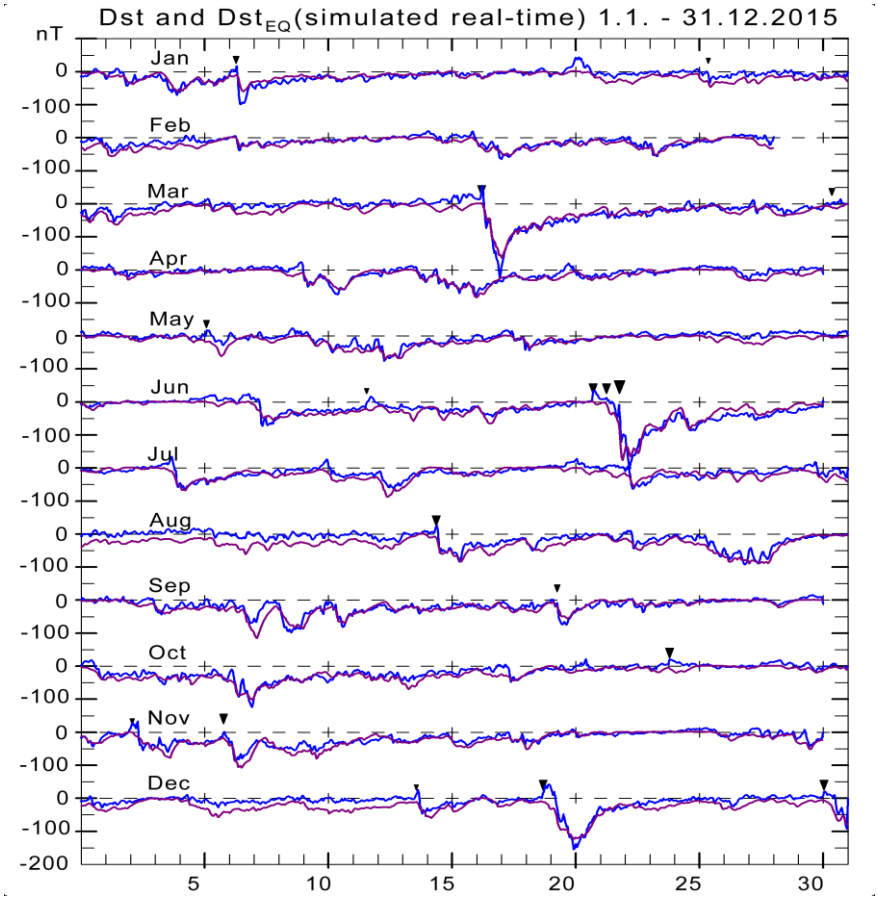

Fig. 8. Real Dst values (blue line) and simulated real-time $Dst_{EQ,SRT}$ values (magenta line) as the interim result for 2015 derived by integration of the simulated real-time PCC-based source function since 2009 without attachment to real Dst values.

The display of $Dst_{EQ,SRT}$ based on simulated real-time PCC indices in Fig. 8 is almost indistinguishable from the corresponding diagram of Dst_{EQ} based on post-event PCC values presented in Fig. 15b of Stauning (2020c). The post-event and the simulated real-time PCC index values differ only by small and randomly distributed contributions. For a more comprehensive illustration, the Appendix presents in Figs. A3-A4 further displays throughout 2011-2018 of Dst and values of $Dst_{EQ,SRT}$ calculated from using PCC_{SRT} in the source function and integrated since 2009 without attachment to the real Dst values.

These calculations generate Dst gradients in simulated real-time which upon integration provide the Dst indices up one hour ahead. They illustrate the results made possible by calculations of Dst indices from a PCC-based source function with continuous access to PC indices in real time. The process operates much like the forecast of Dst values (e.g. at Space Weather centres) based on data arriving from remote spacecrafts in the solar wind.

8.4. Predictability of ring current intensities derived from polar cap indices.

Generally, the ring current intensities defined by the Dst or SYM-H indices start increasing when the gradient in Eq. 6 assumes negative values as the PCC indices rise above zero. There is no apparent threshold value. The Dst_{EQ} index value continue increasing its negative amplitude as long as the gradient in Eq. 6 is negative and may reach peak minimum at zero gradients even in cases

where the PC indices are still large and rising. The ring current intensities decay when the gradient term in Eq. 6 assumes positive values when the PCC-bases source term becomes (numerically) smaller than the decay function term.

An important question is the predictability of the Dst (or SYM-H) values. The fair agreement between real and simulated real-time Dst_{EQ} values ensures that the PCC-based expression in Eq. 6 provides the actual Dst gradient. Thus, the Dst value could be estimated one hour ahead from its present value with fair precision. The Dst index values could not be estimated reliably beyond one hour ahead from observed series of PC index values.

It is believed that running a reliable operational estimate of ring current intensities one hour ahead could be a useful supplement to predictions of Dst values from space data derived from satellites such as the ACE satellite in the solar wind (e.g., O'Brian and McPherron, 2000; Lundstedt et al., 2002).

Considering the data collection from remote polar observatories in the harsh arctic environment, the reliability might be enhanced by establishing access to polar magnetic data from multiple sources (Stauning, 2018b). Thus, data from Resolute Bay (RES) might substitute for data from the standard observatory, Qaanaaq, for PCN values, while data from Dome-C could be substituted for data from the standard observatory, Vostok, for PCS values. The scaling coefficients should be taken from observatory-specific tables. The reference levels should be derived using the HSRW QDC scheme. Specifications of on-line derivation of PC index values are provided in the appendix to Stauning (2018c)

With the small contributions to the ring current indices from magnetopause currents (MPC) fixed at 20 nT, then the Dst (or SYM-H) indices could be derived with slightly reduced accuracy from the simplified version of Eq. 6 shown in Eq. 8, using the modified parameters from Stauning (2020c):

$$d(Dst^*)/dt = gradD \cdot PCCeff - Dst^*/\tau \quad (8)$$

where

$Dst^* = Dst - 20$ nT

$gradD = -4.5$ nT/(mV/m)

$PCCeff = PCC$ if $PCC < 5$ mV/m or $PCCeff = PCC + 0.6 \cdot (PCC - 5)$ if $PCC > 5$ mV/m

$\tau = 5.5$ h if $Dst < -52$ nT or $\tau = 7.0$ h if $Dst > -52$ nT

The integration of Eq. 8 could be conducted in steps of one or a few (up to 5) minutes.

9. Discussions

Investigations aiming at deriving intensities of the solar wind merging electric field, E_M (Kan and Lee, 1979), from polar cap indices (e.g., Gao et al., 2012; Troshichev and Andrezen, 1985; Troshichev and Lukianova, 2002; Troshichev and Sormakov, 2015, 2018, 2019; Troshichev et al., 2011b) might take advantage of the improved correlation available with the PCC indices over the individual PCN or PCS indices or other possible combinations such as their averages or the summer or winter PC index selection. This approach solves for the conceptual problem in having two at times quite different index values available for estimates of the energy arriving to the magnetosphere from the impinging solar wind. Using the PCC indices also avoids negative PC index values which could definitely not substitute for the non-negative merging electric field values.

Previous investigations have attempted to link ring current intensities to further observable solar wind or geospace parameters. The approach by Burton et al. (1975), which has provided basis for

the method applied here, used the Y-component of the solar wind electric field to estimate ring current intensities defined by the Dst index.

Including further solar wind parameters and using neural network technique, the work by O'Brien and McPherron (2000) have analysed ring current dynamics aiming at forecasting the development of the ring current index Dst in real time based on ACE measurements at the L1 liberation orbit. In a similar approach Lundstedt et al. (2002) applied neural network for operational forecasts of the Dst indices from solar wind parameters without attachment to recorded Dst values. These comprehensive approaches have provided valuable insight in the role of various solar wind parameters and the processes responsible for the solar wind-magnetosphere interactions.

Stepanova et al. (2005) developed procedures for prediction of Dst variations 1 hour ahead from polar cap indices. The neural network in different versions used 3 sets of input parameters, 24 previous hourly averages of 1-min polar cap PCN indices, 24 previous hourly PCN standard deviation values, and 24 previous Dst values. The two versions based exclusively on PC indices appeared to saturate early at a predicted Dst level of around 75 nT even for cases of observed Dst values up to 120 nT. The third version attached also to the previous 24 real Dst values performed better than that to reach predicted values one hour ahead close to the observed Dst indices with standard deviations on the order of 15 nT judged from their Fig. 2.

Further reports of the relations between polar cap and ring current indices have been published by Troshichev et al. (2011a), Troshichev and Janzhura (2012), Troshichev (2017) and Troshichev and Sormakov (2018). An extract of these works have been included in the ISO/TR23989:2020 technical report issued by the International Standards Organisation (ISO). However, the report is haunted by trivial errors and several of its statements are misleading or incorrect. Much of the confusion arrives from the attempts to link total ring current indices, Dst or SYM-H, directly with the polar cap PC indices.

In spite of the expressed importance for real-time Space Weather applications none of the quoted publications actually uses real-time (or simulated real-time) PC indices in their presentations. The IAGA-recommended near-real time PCN and PCS indices have been available since February 2014 from the AARI web site http://pcindex.org and also for some years from the web portal https://isgi.unistra.fr of the International Service for Geomagnetic Indices (ISGI) supported by IAGA. In spite of several requests it has not been possible to obtain recordings of the near-real time index values issued to the scientific community from these web sites over the years. It is even kept secret (not responding to specific requests) whether or not the published near-real time PC indices are actually recorded and kept.

10. Summary.

10.1 Correlation of PC indices with solar wind merging electric field intensities.

It has been demonstrated (Fig. 3) that the non-negative combination, PCC, of the PCN and PCS indices have closer relations to the merging electric field, E_M, in the solar wind with considerably higher correlation coefficients that either of the individual PC indices and further possible combinations.

The naming of the combined PCN and PCS indices, PCC (Eq. 4), enables a well-defined distinguishing between this index combination and other possible combinations or selections of PCN and PCS indices often just named "PC index". Thus from published works:

Troshichev et al. (2011a): selection of local summer PC index values (PCU).

Troshichev et al. (2011b): PCN indices.

Troshichev et al. (2011c): PCN and PCS. PC index in statistics not defined.

Troshichev and Janzhura (2012): selections of local winter (PCW) and summer (PCU) indices.

Troshichev et al. (2012): PCN, PCS, local summer (PCU) and local winter (PCW) PC selections.

Troshichev et al. (2014): PCN and PCS. PC index in statistics not defined.

Troshichev and Sormakov (2015, 2018): Average of PCN and PCS (PCA).

A more comprehensive analysis of the relations between E_M and various PC index series including the plain average of PCN and PCS and the selection of summer or winter PC indices and also the correlation with the Kp index and the partial ring current indices, ASY-H, is provided in Stauning (2020c). Table 5 from this work is quoted in Table 4 here. The correlation coefficients for epoch 1996-2016 noted in Table 4 agree well with those estimated here in the post-event version for epoch 2009-2018 as noted in Tables 1 and 2.

Table 4. Post-event **c**orrelation coefficients for epoch 1996 – 2016. (Table 5 of Stauning, 2020c)

Correlation	PCC	PCN	PCS	PCA[1)]	PCW[2)]	PCU[3)]
E_M	**0.764**	0.714	0.727	0.720	0.732	0.707
Kp	**0.820**	0.756	0.764	0.791	0.799	0.729
ASY-H[4)]	**0.743**	0.702	0.679	0.716	0.700	0.683

[1)] : Average of PCN and PCS

[2)] : Selection of winter hemisphere PC indices

[3)] : Selection of summer hemisphere PC indices

[4)] : Storm events

Thus, the present work confirms that PCC indices are superior over the hemispherical PC indices or further index combinations in applications involving the E_M parameter in the solar wind or global geomagnetic disturbances such as magnetospheric substorms and ring current developments because of their response to magnetic activity in both polar caps and the adequate handling of negative PC index values.

However, the unipolar PCN or PCS indices could still be the better choice for studying relations to geomagnetic phenomena confined predominantly to the individual polar caps, such as upper atmosphere auroral heating and reverse plasma convection during NBZ conditions.

10.2. Direct correlation of PC indices with 1-min SYM-H and ASYM-H indices.

For the relations between the PC indices and the SYM-H and ASY-H indices there are coarse agreement between their averages taken over 6-12 hours. For the more detailed variations on scales of one or a few hours, the ASY-H indices still to some extent show changes that reflect the variations seen in the PC indices while the SYM-H (and Dst) indices display almost no response. Thus, the ASY-H indices display some of the features seen in the PC indices while the direct correlation of PC indices with SYM-H indices appears not being meaningful.

10.3. Relations of PC indices to Dst or hourly averages of SYM-H.

It has been demonstrated that integration of a source function based on the non-negative PCC index combination (Eq. 4), may provide equivalent Dst or SYM-H values that rather closely agree with

observed (real) index values in real time applications (Figs. 7a,b and 8). The PC-based source function may provide the actual Dst gradient in real-time which would then define the total ring current intensities (Dst or SYM-H indices) up to one hour ahead. The ring current developments beyond one hour could not be predicted reliably from observed PC index values.

The neural-network-based techniques may provide important information on the relations between geomagnetic storms and solar wind conditions. It appears that this technique may provide forecasts of ring current intensities about one hour ahead of the arrival of processed spacecraft data from satellites in the solar wind. The simple and reliable polar cap indices may provide a worthwhile supplement to space-data based estimates of geomagnetic storm developments.

Conclusions

- The "DMI2016" derivation methods used to calculate PC index values whether post-event or in real time are accurate and reliable and also well documented.

- The PC indices, particularly in the non-negative PCC index combination, have close relations with the merging electric fields (E_M) in the solar wind assumed to control the input of energy from the solar wind to the magnetosphere.

- The partial ring current intensities characterized by the ASY-H indices relate directly to the PC indices with the closest correlation observed with the PCC index version over the individual PCN or PCS indices or further combinations.

- The total ring current intensities characterized by the Dst and SYM-H indices start rising when the PCC-based source function assumes negative values when either or both PCN and PCS indices are positive. There is not observed specific PCN or PCS threshold values.

- The total ring current intensities (Dst, SYM-H) start decaying when the source function assumes positive values in the balance between contributions derived from the PC indices and the exponential decay function. The decay may start at any PC index level even at increasing PC index values.

- Earlier attempts to link the peak times and amplitudes of ring current indices, Dst or SYM-H, to the times and amplitudes of PC index maxima should be replaced by integration of the PC-based ring current source function which in real-time versions may provide good indications of ring current developments up to 1 hour beyond actual time.

- Integration of the PCC-based source function throughout the decade from 2009 to 2018 by using simulated real-time PC index values have provided equivalent Dst index values very close to the real Dst indices.

- The close relations between transpolar convection of plasma with embedded magnetic fields characterized by the PC indices and the building of the total as well as the partial ring currents might provide further insight in magnetospheric energy exchange and disturbances processes related to solar wind-magnetosphere interactions.

- The polar cap indices represent the input of energy from the solar wind to the Earth's magnetosphere and are valuable assets for Space Weather applications, particularly in their real-time versions.

Data availability:

PCN and PCS index series derived by the IAGA-endorsed procedures are available through AARI and ISGI web sites. Archived PCN and PCS data used in the paper were downloaded from http://isgi.unistra.fr web portal in January 2020 unless otherwise noted. The web site, http://pcindex.org, holds PCN and PCS index coefficients and includes the descriptive document "Polar Cap (PC) Index" (Troshichev, 2011).

Geomagnetic data from Qaanaaq, Vostok, and Dome-C observatories were downloaded from the INTERMAGNET data service web portal at http://intermagnet.org. Ring current indices, Dst, SYM-H and ASY-H were downloaded from the web portal for World Data Centre WDC-C2 in Kyoto at http://swdcwww.kugi.kyoto-u.ac.jp/dstdir/index.html. Spacecraft data needed to generate the merging electric field values were downloaded from the OMNIweb service portal http://omniweb.gsfc.nasa.gov. SSC data were downloaded from the ISGI data service portal http://isgi.unistra.fr .

The magnetic observatory in Qaanaaq is managed by the Danish Meteorological Institute, while the magnetometer instruments are operated by DTU Space, Denmark. The Vostok observatory is operated by the Arctic and Antarctic Research Institute in St. Petersburg, Russia. The Dome-C observatory is managed by Ecole et Observatoire des Sciences de la Terre (France) and Istituto Nazionale di Geofisica e Vulcanologia (Italy).

The "DMI2016" PC index version is documented in the report SR-16-22 (Stauning, 2016) available at the web site: http://www.dmi.dk/fileadmin/user_upload/Rapporter/TR/2016/SR-16-22-PCindex.pdf

Acknowledgments. The staffs at the observatories in Qaanaaq (Thule), Vostok, and Dome-C, and their supporting institutes are gratefully acknowledged for providing high-quality geomagnetic data for this study. The provision of space data from the IMP, ACE, Wind, and Geotail missions and the management of data by the OMNIweb service, the supply of geomagnetic data from the INTERMAGNET data service centre, and the excellent performance of the ISGI and AARI PC index portals are greatly appreciated. The efforts from the geomagnetic observatories involved in the collection of data for the Dst, SYM, and ASY indices and the processing at WDC-C2 in Kyoto is most gratefully acknowledged. The author gratefully acknowledges the collaboration and many rewarding discussions in the past with Drs. O. A. Troshichev and A. S. Janzhura at the Arctic and Antarctic Research Institute in St. Petersburg, Russia.

References

Burton R. K, McPherron R. L, & Russell C. T. (1975). An empirical relationship between interplanetary conditions and Dst. *J Geophys Res 80*, 4204-4214. https://doi.org/10.1029/JA080i031p04204.

Chambodut A., Di Mauro D., Schott J. J., Bordais P., Agnoletto L., & Di Felice P. (2009). Three years continuous record of the Earth's magnetic field at Concordia station (Dome-C, Antarctica). *Annals of Geophysics 52*, 15-24. https://doi.org/10.4401/ag-4569 .

Dessler, A. J. & Parker, E. N. (1959). Hydromagnetic theory of geomagnetic storms. *J Geophys Res 64*, 2239-2259. https://doi.org/10.1029/JZ064i012p02239.

Di Mauro D., Cafarella L., Lepidi S, Pietrolungo M, Alfonsi L, Chambodut A. (2014). Geomagnetic polar observatories: the role of Concordia station at Dome C, Antarctica, *Annals of Geophysics 57, 6*, G0656. https://doi.org/10.4401/ag-6605 .

Dungey J. W. (1961). Interplanetary Magnetic Field and the Auroral Zones. *Phys Rev Lett 6***,** 47-48. https://doi.org/10.1103/PhysRevLett.6.47 .

Feldstein, Y. I., Pisarsky, V. Yu., Rudneva, N. M. & Grafe, A. (1984). Ring current simulation in connection with interplanetary space conditions. *Planet Space Sci 32*. 975-984. https://doi.org/10.1016/0032-0633(84)90054-0.

Gao, Y., Kivelson, M. G., & Walker, R. J. (2012). The linear dependence of polar cap index on its controlling factors in the solar wind and magnetotail. *J Geophys Res, 117* (A5). https://doi.org/10.1029/2011JA017229 .

IAGA Resolution no. 3 (2013). http://www.iaga-aiga.org/resolutions.

Iyemori, T., Araki, T., Kamei, T., & Takeda, M. (2000). Mid-latitude geomagnetic indices "ASY" and "SYM" for 1999. *Geomagnetic indices home page*, ed.: T. Iyemori, WDC-C2 for Geomagnetism, Kyoto University. http://swdcwww.kugi.kyoto-u.ac.jp/dstdir/index.html

Janzhura, A. S. & Troshichev, O. A. (2011). Identification of the IMF sector structure in near-real time by ground magnetic data. *Annales Geophysicae, 29*, 1491-1500. https://doi.org/10.5194/angeo-29-1491-2011 .

Jorgensen AM, Spence HE, Hughes WJ, Singer HJ. 2004. A statistical study of the ring current. *J Geophys Res 109* A12204. https://doi.org/10.1029/2003JA010090 .

Kan, J. R. & Lee, L. C. (1979). Energy coupling function and solar wind-magnetosphere dynamo. *Geophysical Research Letter*, 6 (7)**,** 577- 580. https://doi.org/10.1029/GL006i007p00577 .

Kappenman, J. (2010). Geomagnetic storms and their impact on the U.S. power grid. Metatech Report, Meta-R-319, 197 pp. Available at https://www.ferc.gov/industries/electric/indus-act/reliability/cybersecurity/ferc_meta-r-319.pdf

Lundstedt, H., Gleisner, H. & Wintoft, P. (2002). Operational forecasts of the geomagnetic Dst index. *Geophys. Res. Lett. 29(24)*, 218. https://doi.org/10.1029/2002GL016151

Matzka, J. (2014). PC_index_description_main_document_incl_Appendix_A.pdf. Available at DTU Space web portal: ftp://ftp.space.dtu.dk/WDC/indices/pcn/

Nielsen, J. B. & Willer, A. N. (2019). Restructuring and harmonizing the code used to calculate the Definitive Polar Cap Index. *Report from DTU Space*. https://tinyurl.com/sx3g5t5

Pulkkinen, A., Bernabeu, E., Thomson, A. et al. (2017). Geomagnetically induced currents: Science, engineering, and applications readiness. *Space Weather*, *15*, 828– 856, https://doi.org/10.1002/2016SW001501 .

O'Brien, T. P. & McPherron, R. L. (2000). Forecasting the ring current index Dst in real time, *J. Atmos Solar-Terr Phys 62*, 1295-1299. https://doi.org/10.1016/S1364-6826(00)00072-9

Pulkkinen, A., Bernabeu, E., Thomson, A. et al. (2017). Geomagnetically induced currents: Science, engineering, and applications readiness. *Space Weather*, *15*, 828– 856, https://doi.org/10.1002/2016SW001501 .

Sckopke, N. (1966). A general relation between the energy of trapped particles and the disturbance field near the Earth, *J Geophys Res 71* 3125-3130. https://doi.org/10.1029/JZ071i013p03125

Stauning, P. **(**2007). A new index for the interplanetary merging electric field and the global geomagnetic activity: Application of the unified Polar Cap (PCN and PCS) indices. *AGU Space Weather*, *5*, S09001. https://doi.org/10.1029/2007SW000311.

Stauning, P. (2011). Determination of the quiet daily geomagnetic variations for polar regions. *J. Atmos Solar-Terr Phys, 73(16)*, 2314-2330. https://doi.org/10.1016/j.jastp.2011.07.004 .

Stauning, P. (2012). The Polar Cap PC Indices: Relations to Solar Wind and Global Disturbances, Exploring the Solar Wind, Marian Lazar (Ed.). *InTech Publ*. ISBN: 978-953-51-0339-4. https://doi.org/10.5772/37359

Stauning P. (2013). Power grid disturbances and polar cap index during geomagnetic storms, *J Space Weather Space Clim 3* A22. https://doi.org/10.1051/swsc/2013044 .

Stauning, P. (2015). A critical note on the IAGA-endorsed Polar Cap index procedure: effects of solar wind sector structure and reverse polar convection. *Annales Geophysicae, 33***,** 1443-1455. https://doi.org/10.5194/angeo-33-1443-2015 .

Stauning, P. (2016). The Polar Cap (PC) Index.: Derivation Procedures and Quality Control. *DMI Scientific Report SR-16-22*. Available at: https://www.dmi.dk/fileadmin/user_upload/Rapporter/TR/2016/SR-16-22-PCindex.pdf .

Stauning, P. (2018a). A critical note on the IAGA-endorsed Polar Cap (PC) indices: excessive excursions in the real-time index values. *Ann Geophys 36*, 621–631. https://doi.org/10.5194/angeo-36-621-2018 .

Stauning, P. (2018b). Multi-station basis for Polar Cap (PC) indices: ensuring credibility and operational reliability. *J Space Weather Space Clim 8*, A07. https://doi.org/10.1051/swsc/2017036 .

Stauning, P. (2018c). Reliable Polar Cap (PC) indices for space weather monitoring and forecast, *J Space Weather Space Clim 8***,** A49. https://doi.org/10.1051/swsc/2018031

Stauning, P. (2020a). Using PC indices to predict violent GIC events threatening power grids. *J Space Weather Space Clim 10* A3. https://doi.org/10.1051/swsc/2020004 .

Stauning, P. 2020b. The Polar Cap (PC) index: invalid index series and a different approach. *Space Weather* 16, e2020SW002442. https://doi.org/10.1029/2020SW002442

Stauning, P. (2020c). The Polar Cap (PC) index combination, PCC: relations to solar wind properties and global magnetic disturbances. *J Space Weather Space Clim* https://doi.org/10.1002/essoar.10505338.1. (accepted for publication).

Stauning, P., Troshichev, O. A., & Janzhura, A. S. (2006). Polar Cap (PC) index. Unified PC-N (North) index procedures and quality. *DMI Scientific Report, SR-06-04*. (revised 2007 version available at http://www.dmi.dk/fileadmin/Rapporter/SR/sr06-04.pdf).

Stauning, P., Troshichev, O. A., & Janzhura, A. S. (2008). The Polar Cap (PC) index: Relations to solar wind parameters and global activity level, *J Atmos Solar-Terr Phys 70(18)*, 2246-2261. https://doi.org/10.1016/j.jastp.2008.09.028 .

Stepanova, M., Anatova, E. & Troshichev, O. A. (2005). Prediction of Dst variations from Polar Cap indices using time-delay neural network, *J Atmos Solar-Terr Phys 67*, 1658-1664. https://doi.org/10.1016/j.jastp.2005.02.027 .

Sugiura, M. & Kamei, T. (1981). Description of the hourly Dst index, in: *Geomagnetic indices home page*, ed. T. Iyemori, WDC-C2 for Geomagnetism, Kyoto University. http://swdcwww.kugi.kyoto-u.ac.jp/dstdir/index.html

Troshichev, O. A. (2011). Polar Cap (PC) Index. Available at: http://pcindex.org (see Supported materials).

Troshichev, O. A. (2017). Polar cap magnetic activity (PC index) and space weather monitoring, *Édition universitaires européennes*, ISBN: 978-3-8381-8012-0.

Troshichev, O. A. & Andrezen, V. G. (1985). The relationship between interplanetary quantities and magnetic activity in the southern polar cap, *Planet. Space Sci*., *33*, 415-419.

741 Troshichev, O. A. & Janzhura, A. S. (2012). Physical implications of discrepancy between summer and
742 winter PC indices observed in the course of magnetospheric substorms. *Advances in Space Research, 50*
743 (1), 77-84. https://doi.org/10.1016/j.asr.2012.03.017

744 Troshichev, A. O. & Lukianova, R. Y. (2002). Relation of PC index to the solar wind parameters
745 and substorm activity in time of magnetic storms, *J Atmos Solar-Terr Phys, 64*, 585.
746 https://doi.org/10.1016/S1364-6826(02)00016-0 .

747 Troshichev, O. A. & Sormakov, D. A. (2015). PC index as a proxy of the solar wind energy that
748 entered into the magnetosphere : (2) Relation to the interplanetary electric field E_{KL}. *Earth,*
749 *Planets Space 67*, 170. https://doi.org/10.1186/s40623-015-0338-4 .

750 Troshichev, O. A. & Sormakov, D. A. (2018). PC index as a proxy of the solar wind energy that
751 entered into the Magnetosphere: 3. Development of magnetic storms, *J Atmos Solar-Terr Phys*
752 *180*, 60-77. https://doi.org/10.1016/j.jastp.2017.10.012

753 Troshichev, O. A. & Sormakov, D. A. (2019). PC index as a proxy of the solar wind energy that entered into
754 the magnetosphere: (5) verification of the solar wind parameters presented at OMNI website. *J Atmos*
755 *Solar-Terr Phys 196*. https://doi.org/10.1016/j.jastp.2019.105147

756 Troshichev, O. A., Andrezen, V. G., Vennerstrøm, S. & Friis-Christensen, E. (1988). Magnetic
757 activity in the polar cap – A new index. *Journal of Planetary and Space Sciences 36(11)*, 1095-
758 1102. https://doi.org/10.1016/0032-0633(88)90063-3

759 Troshichev, O., Somarkov, D. & Janzhura, A. S. (2011a). Relation of PC index to the geomagnetic
760 storm Dst variation, *J Atmos Solar-Terr Phys 73*, 611-622.
761 ttps://doi.org/10.1016/j.jastp.2010.12.015

762 Troshichev, O. A., Podorozhkina, N. A., & Janzhura, A. S. (2011b). Invariability of relationship
763 between the polar cap magnetic activity and geoeffective interplanetary electric field. *Ann*
764 *Geophys 29*, 1479-1489. https://doi.org/10.5194/angeo-29-1479-2011 .

765 Troshichev, O., D. Sormakov, A. Janzhura (2012), Sawtooth substorms generated under conditions of the
766 steadily high solar wind energy input into the magnetosphere: relationship between PC, AL, and ASYM
767 indices, *Adv Space Res 49*, 872-882. https://doi.org/10.1016/j.asr.2011.12.011

768 Troshichev, O. A. , Podorozhkina, N. A., Sormakov, D. A., & Janzhura, A. S. (2014). PC index as a proxy of
769 the solar wind energy that entered into the magnetosphere: 1. Development of magnetic substorms. *J*
770 *Geophys Res Space Physics, 119*. https://doi.org/10.1002/2014JA019940 .

771 Vennerstrøm, S. (1991). The geomagnetic activity index PC, PhD Thesis, Scientific Report 91-3,
772 Danish Meteorological Institute, 105 pp.
773 https://www.dmi.dk/fileadmin/user_upload/Rapporter/SR/1991/sr91-3.pdf

774 Reference is made to the ISO report (2020): Space environment (natural and artificial) –
775 Operational estimation of the solar wind energy input into the Eath's magnetosphere by means of
776 the ground-based polar cap (PC) index. *International Organization for Standardization*, ISO
777 Technical Report ISO/TR/23989-2020. https://www.iso.org/standard/77565.html

778
779

780 **Appendix.**
781
782 **A1. Diagrams and table of related Dst and PCC indices for storm events 2009-2018.**

783 Corresponding Dst, $Dst_{EQ,SRT}$, and PCC_{SRT} indices for 4-days strong (Dst(peak)<-100 nT)
784 geomagnetic storm events are displayed in Figs. A1a-j and A2a-j. The PC index series was derived
785 with the -40 days HSRW real-time QDC version.
786

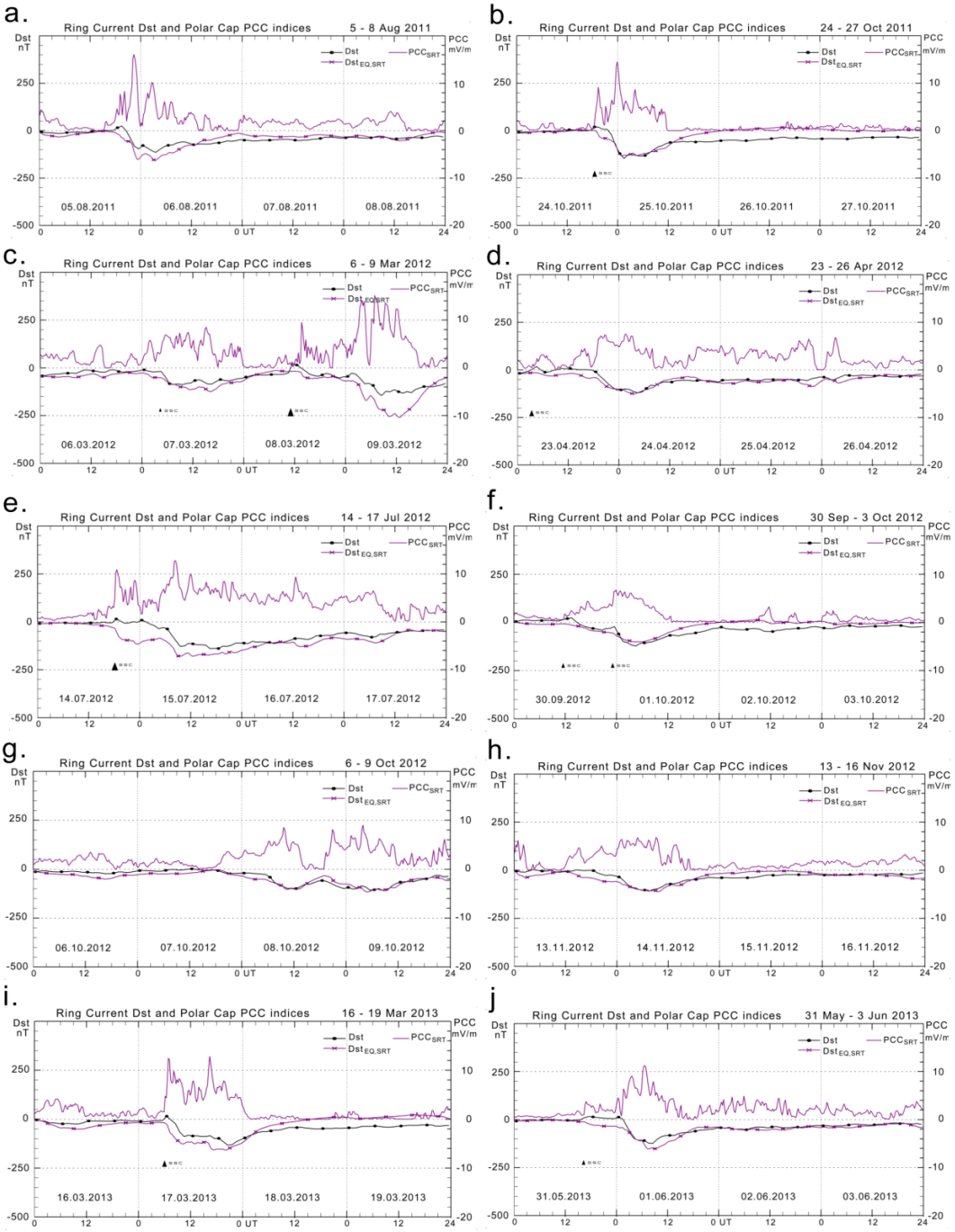

787
788 **Figs. A1a-j.** Examples of published (real) Dst (black line, dots) and equivalent $Dst_{EQ,SRT}$ (magenta, crosses)
789 values in the format like Figs. 7a,b. calculated from using the simulated real-time PCC_{SRT} indices (magenta
790 line) in the source function

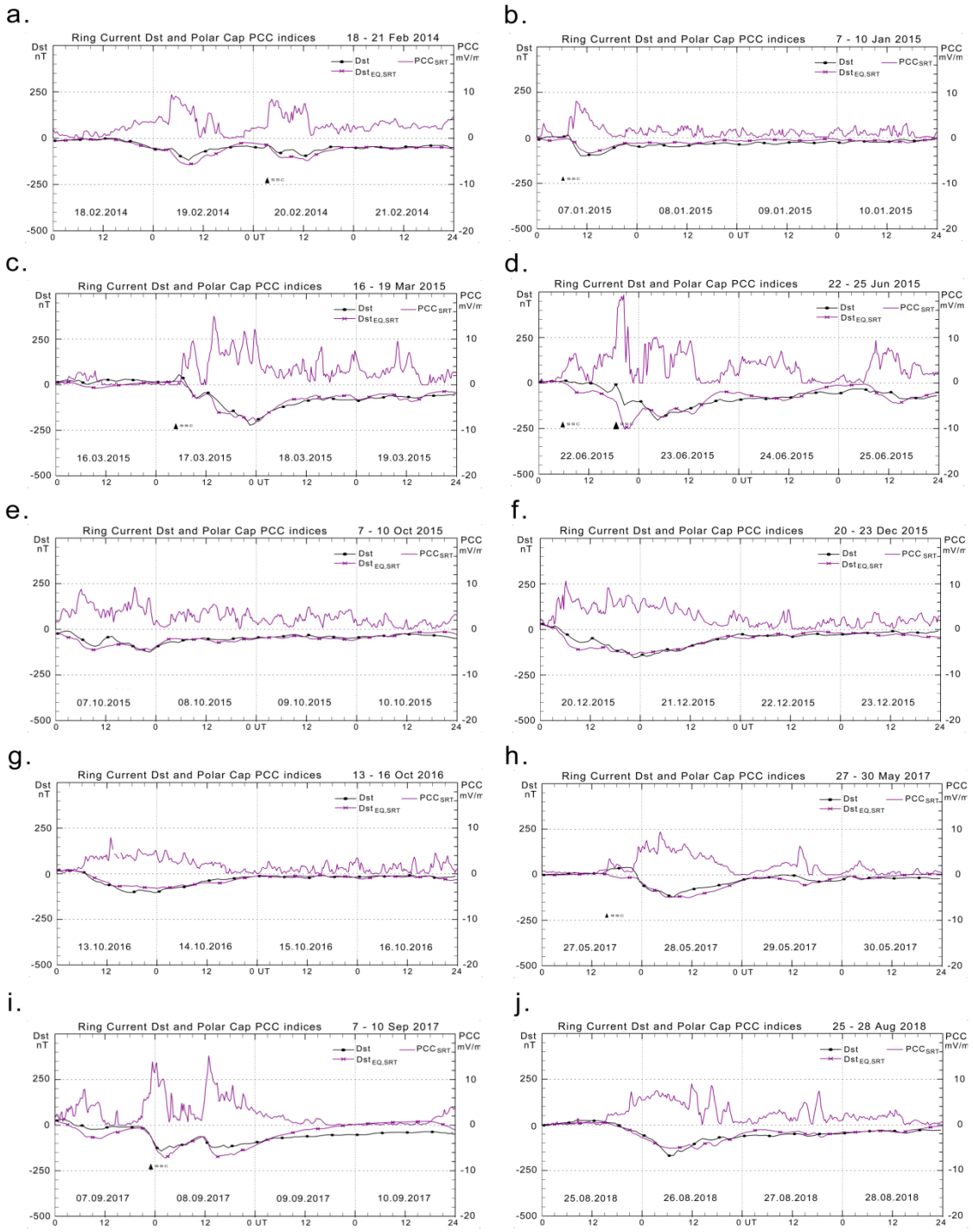

Figs. A2a-j. Examples of published (real) Dst (black line, dots), equivalent $Dst_{EQ,SRT}$ (magenta, crosses), and simulated real-time PCC_{SRT} (magenta).

The examples in Figs. A1a-j and Figs. A2a-j comprise all 4-days intervals of strong magnetic storm events with Dst(peak)<-100 nT occurring between 2009 and 2018 regardless of the actual correlation between Dst and $DstE_{EQ}$. Essential characteristics of the individual events are depicted in Table A1.

Table A1. Characteristics of storm event cases of Dst and PCC_{SRT}-based Dst_{EQ}.

Evnt No.	Date dd.mm.yyyy	Dst_{MIN} nT	$SymH_{MIN}$ nT	$T_{SYMHMIN}$ min[2]	$Dst_{EQ,MIN}$ nT	Corr. coeff.	Avr.dif. nT[1]	Abs.dif. nT[1]	Rms.dif. nT[1]	PCC_{MAX} mV/m	T_{PCCMAX} min[2]
1	05.08.2011	-115	-126	1620	-157	0.772	-0.6	18.3	22.7	17.98	1335
2	24.10.2011	-147	-160	1500	-132	0.748	24.7	31.6	37.1	15.07	1430
3	06.03.2011	-145	-149	4800	-259	0.903	-26.6	29.6	42.0	16.77	4735
4	23.04.2012	-120	-125	1675	-127	0.877	-10.3	14.1	17.6	7.72	1525
5	14.07.2012	-139	-122	2400	-179	0.850	-29.2	29.6	39.8	13.54	1930
6	30.09.2012	-122	-138	1675	-100	0.762	15.0	22.9	26.0	6.91	1430
7	06.10.2012	-109	-116	4800	-116	0.911	-7.6	14.3	16.6	9.59	1445
8	13.11.2012	-108	-117	1855	-111	0.780	-2.5	15.2	18.4	6.85	1725
9	16.03.2013	-132	-131	2640	-158	0.730	7.9	32.3	36.1	12.89	2415
10	31.05.2013	-124	-135	1905	-152	0.887	-10.1	12.8	18.8	11.60	1840
11	18.02.2014	-119	-125	1920	-142	0.915	-7.9	12.5	18.0	9.60	1705
12	07.01.2015	-100	-135	650	-83	0.820	9.5	13.5	16.1	8.65	570
13	16.03.2015	-222	-233	2760	-202	0.960	-2.4	15.7	18.5	16.08	2270
14	22.06.2015	-204	-207	1680	-253	0.775	-4.8	26.8	37.2	20.19	1215
15	07.10.2015	-124	-124	1315	-114	0.832	-5.1	11.4	15.1	9.66	1130
16	20.12.2015	-155	-169	1320	-138	0.935	-4.6	11.8	15.9	11.04	360
17	13.10.2016	-104	-114	1380	-79	0.920	2.4	9.7	12.8	8.27	770
18	27.05.2017	-122	-141	1860	-125	0.864	-7.6	16.3	21.2	9.66	1700
19	07.09.2017	-142	-144	1500	-179	0.765	8.9	35.2	39.6	15.66	2210
20	25.08.2018	-169	-205	1800	-134	0.923	1.9	11.7	16.4	9.18	2150
Avr		-136	-133	2053[3]	-147	0.821	-2.5	19.3	24.3	11.85	1695[3]

Note (1): Average, absolute, and rms differences between Dst and Dst_{EQ} throughout 4 days storm event.

Note (2): The $T_{SYMHMIN}$ and T_{PCCMAX} are times of occurrences in minutes (5 min steps) since start of 4-days interval

Note (3): The numbers are not meaningful by themselves. However, their difference indicates an average delay from PCC_{MAX} to SYM-H_{MAX} of 2053-1695 = 358 min (~ 6 h).

A2. Diagrams of $Dst_{EQ,SRT}$ from integration of PCC_{SRT}-based source function since 2009.

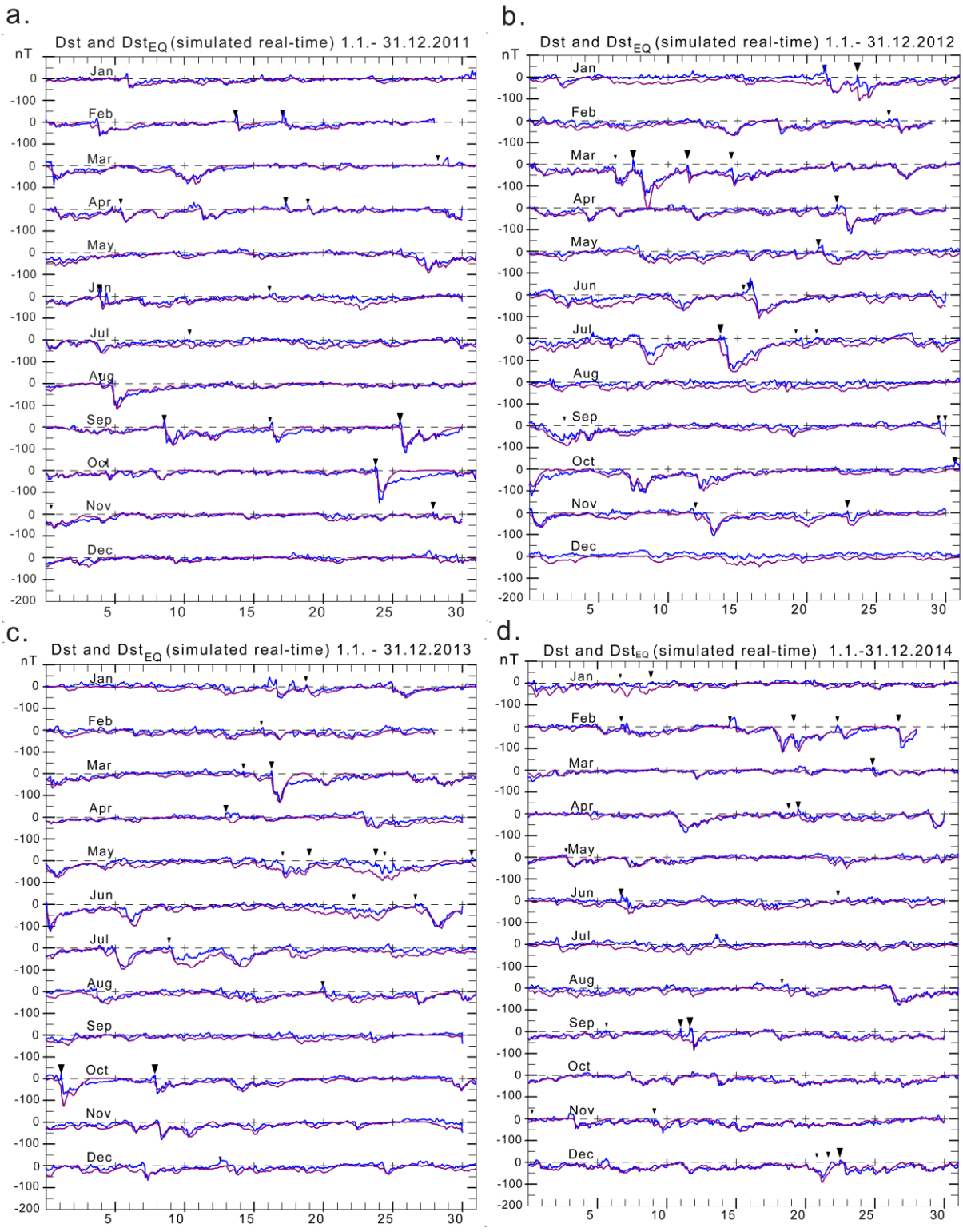

Figs. A3a-d. Real Dst values (blue line) and simulated real-time $Dst_{EQ,SRT}$ values (magenta line) as the interim result for 2011-2014 derived by integration of the simulated real-time PCC_{SRT}-based source function since 2009 without attachment to real (published) Dst values.

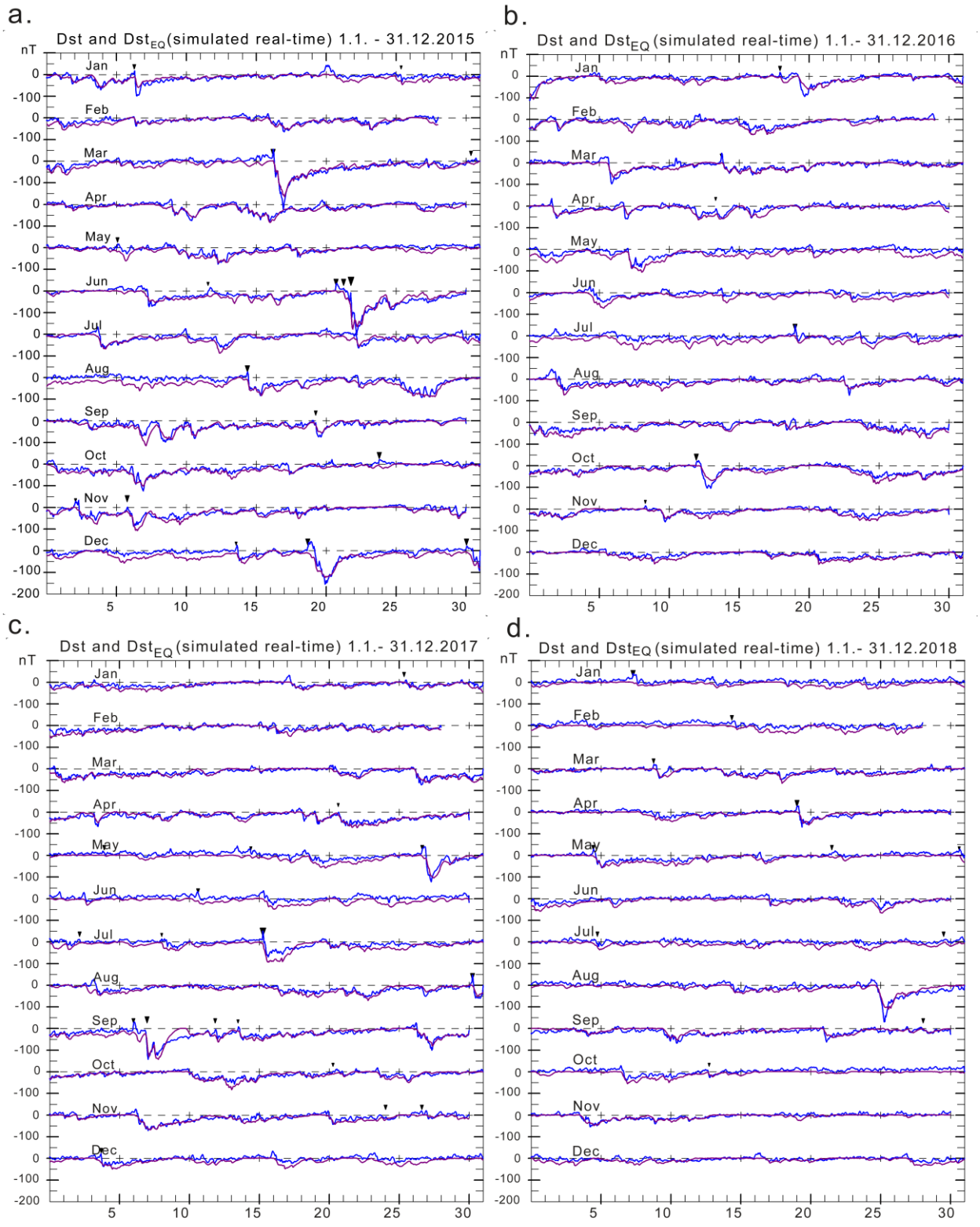

Figs. A4a-d. Real Dst values (blue line) and simulated real-time $Dst_{EQ,SRT}$ values (magenta line) as the interim result for 2015-2018 derived by integration of the simulated real-time PCC_{SRT}-based source function since 2009 without attachment to real (published) Dst values.

Figure 1.

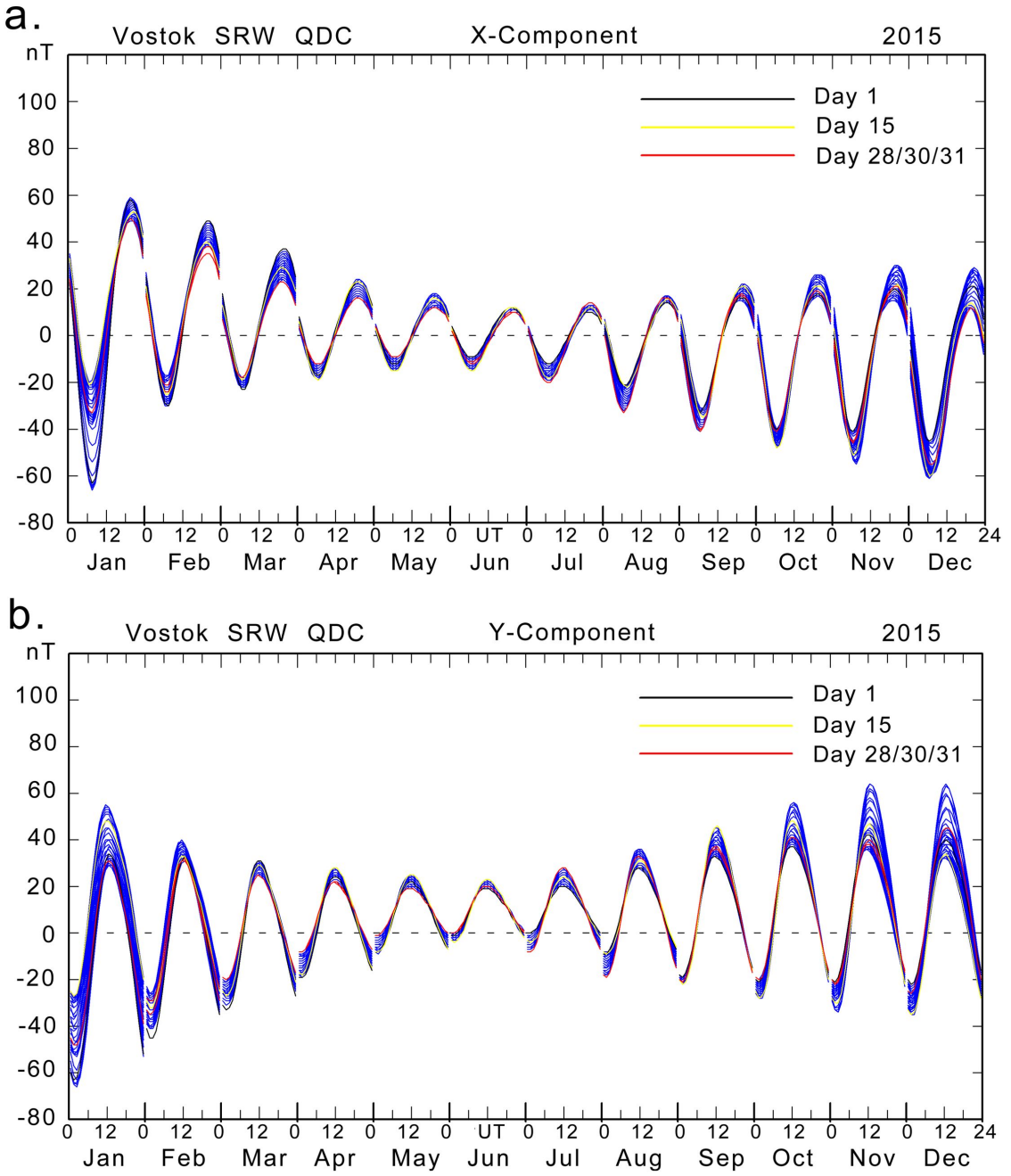
a.
Vostok SRW QDC
X-Component
2015
nT
100
80
60
40
20
0
-20
-40
-60
-80
Day 1
Day 15
Day 28/30/31
0 12 0 12 0 12 0 12 0 12 0 UT 0 12 0 12 0 12 0 12 0 12 0 12 0 12 24
Jan Feb Mar Apr May Jun Jul Aug Sep Oct Nov Dec
b.
Vostok SRW QDC
Y-Component
2015
nT
100
80
60
40
20
0
-20
-40
-60
-80
Day 1
Day 15
Day 28/30/31
0 12 0 12 0 12 0 12 0 12 0 UT 0 12 0 12 0 12 0 12 0 12 0 12 0 12 24
Jan Feb Mar Apr May Jun Jul Aug Sep Oct Nov Dec

Figure 2.

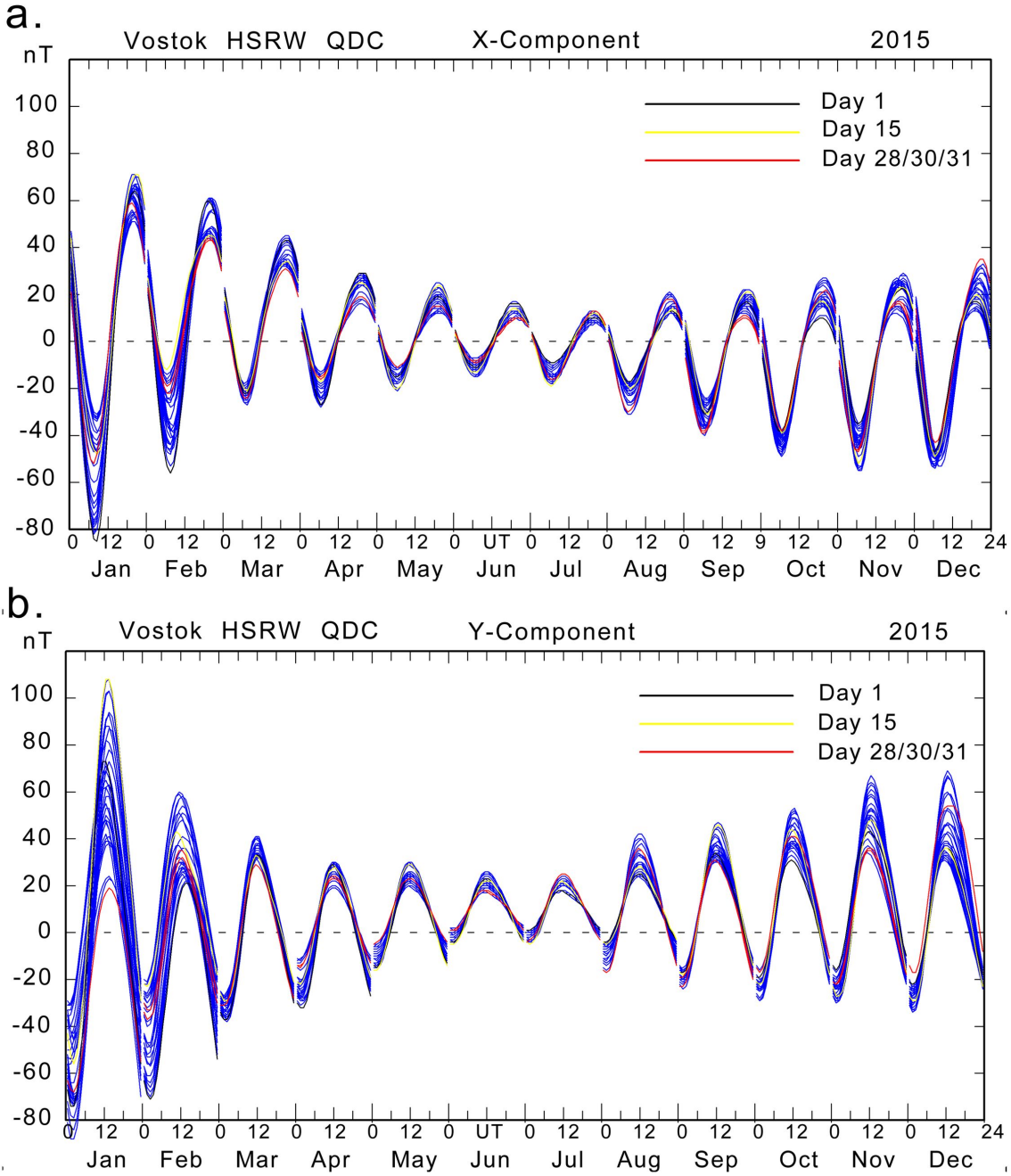
a.
Vostok HSRW QDC
X-Component
2015
nT
100
80
60
40
20
0
-20
-40
-60
-80
Day 1
Day 15
Day 28/30/31
0 12 0 12 0 12 0 12 0 12 0 UT 0 12 0 12 0 12 9 12 0 12 0 12 24
Jan Feb Mar Apr May Jun Jul Aug Sep Oct Nov Dec
b.
Vostok HSRW QDC
Y-Component
2015
nT
100
80
60
40
20
0
-20
-40
-60
-80
Day 1
Day 15
Day 28/30/31
0 12 0 12 0 12 0 12 0 12 0 UT 0 12 0 12 0 12 0 12 0 12 0 12 24
Jan Feb Mar Apr May Jun Jul Aug Sep Oct Nov Dec

Figure 3.

a.

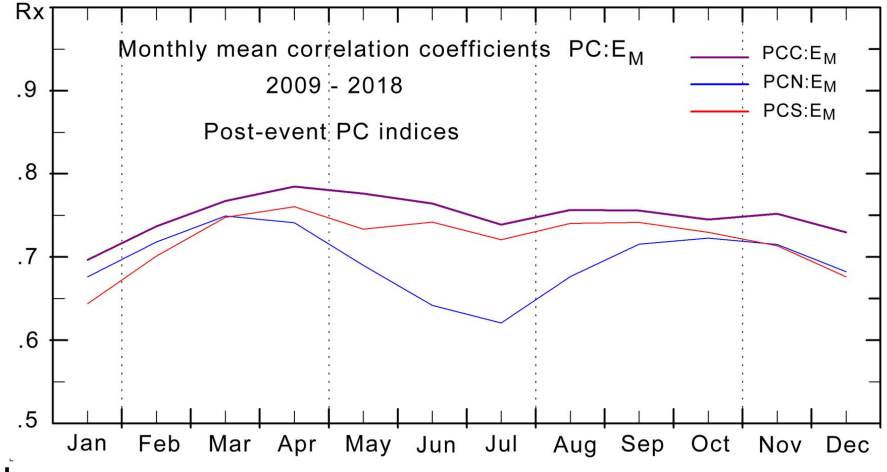
Rx
Monthly mean correlation coefficients PC:E_M
2009 - 2018
Post-event PC indices
PCC:E_M
PCN:E_M
PCS:E_M
.9
.8
.7
.6
.5
Jan
Feb
Mar
Apr
May
Jun
Jul
Aug
Sep
Oct
Nov
Dec

b.

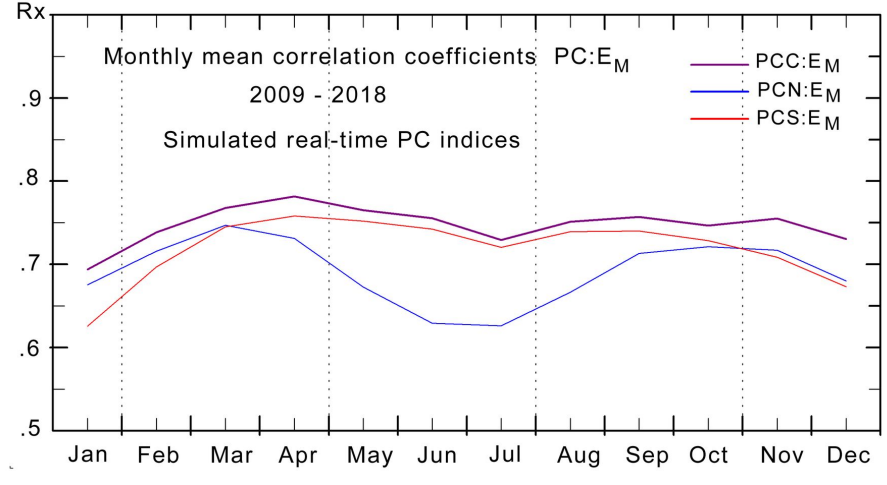
Rx
Monthly mean correlation coefficients PC:E_M
2009 - 2018
Simulated real-time PC indices
PCC:E_M
PCN:E_M
PCS:E_M
.9
.8
.7
.6
.5
Jan
Feb
Mar
Apr
May
Jun
Jul
Aug
Sep
Oct
Nov
Dec

Figure 3.

a.

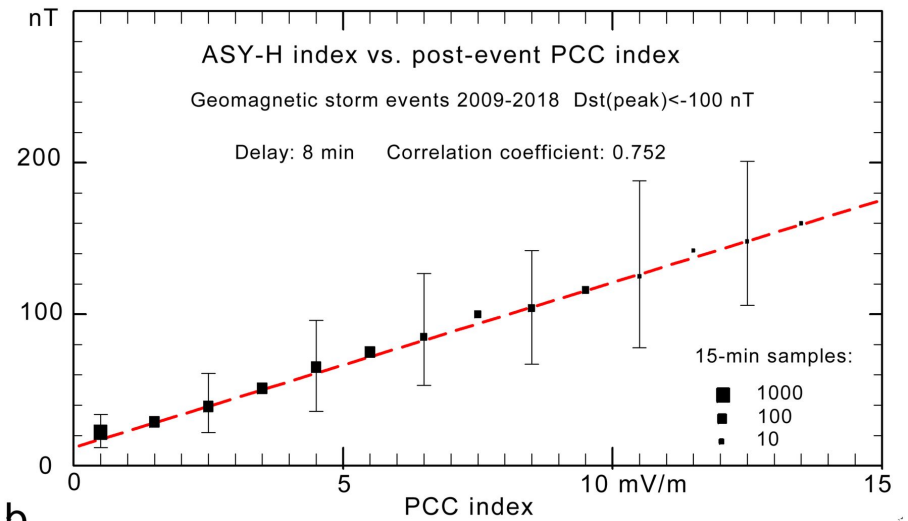
nT
ASY-H index vs. post-event PCC index
Geomagnetic storm events 2009-2018 Dst(peak)<-100 nT
Delay: 8 min Correlation coefficient: 0.752
200
100
0
15-min samples:
1000
100
10
0
5
10 mV/m
15
PCC index

b.

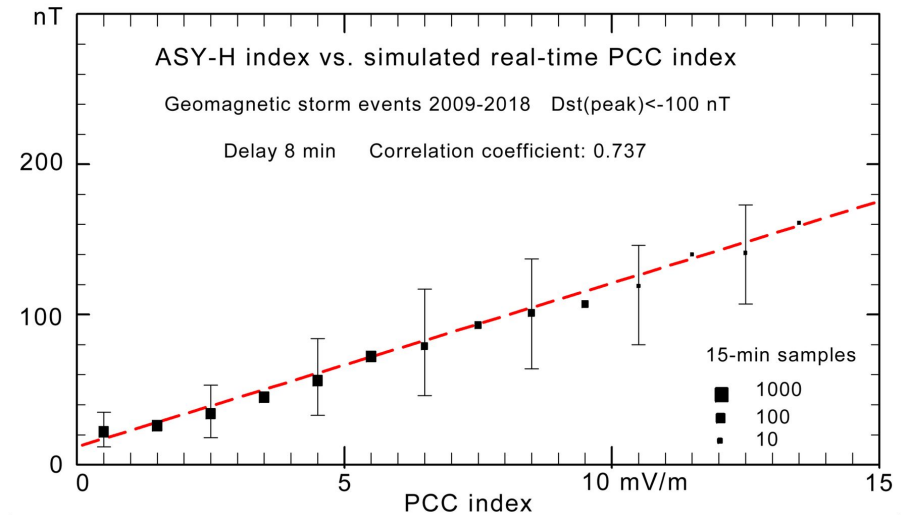
nT
ASY-H index vs. simulated real-time PCC index
Geomagnetic storm events 2009-2018 Dst(peak)<-100 nT
Delay 8 min Correlation coefficient: 0.737
200
100
0
15-min samples
1000
100
10
0
5
10 mV/m
15
PCC index

Figure 5.

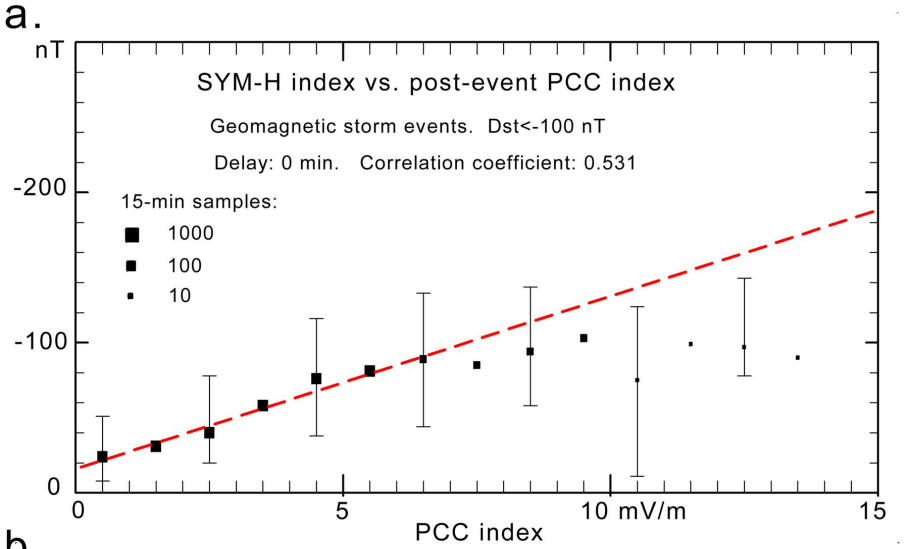
a.
nT
SYM-H index vs. post-event PCC index
Geomagnetic storm events. Dst<-100 nT
Delay: 0 min. Correlation coefficient: 0.531
15-min samples:
1000
100
10
-200
-100
0
0
5
10 mV/m
15
PCC index

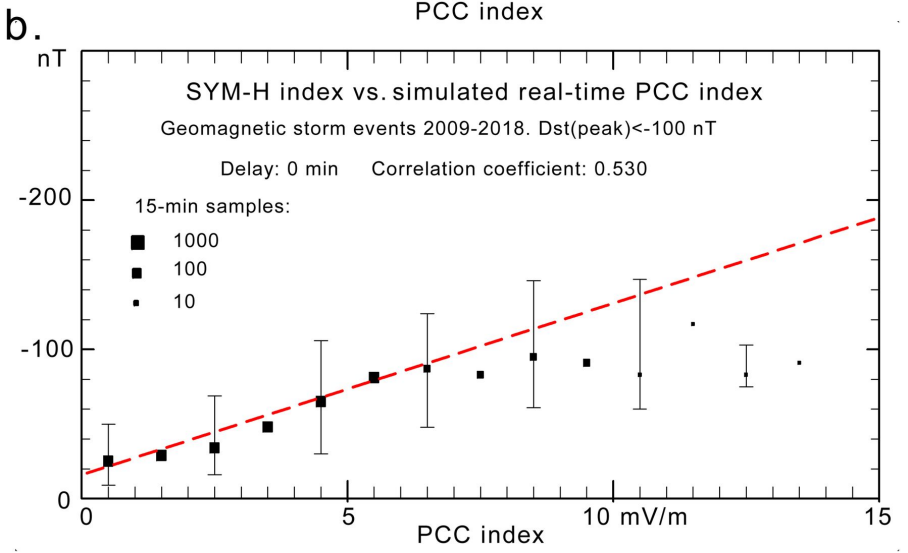
b.
nT
SYM-H index vs. simulated real-time PCC index
Geomagnetic storm events 2009-2018. Dst(peak)<-100 nT
Delay: 0 min Correlation coefficient: 0.530
15-min samples:
1000
100
10
-200
-100
0
0
5
10 mV/m
15
PCC index

Figure 6.

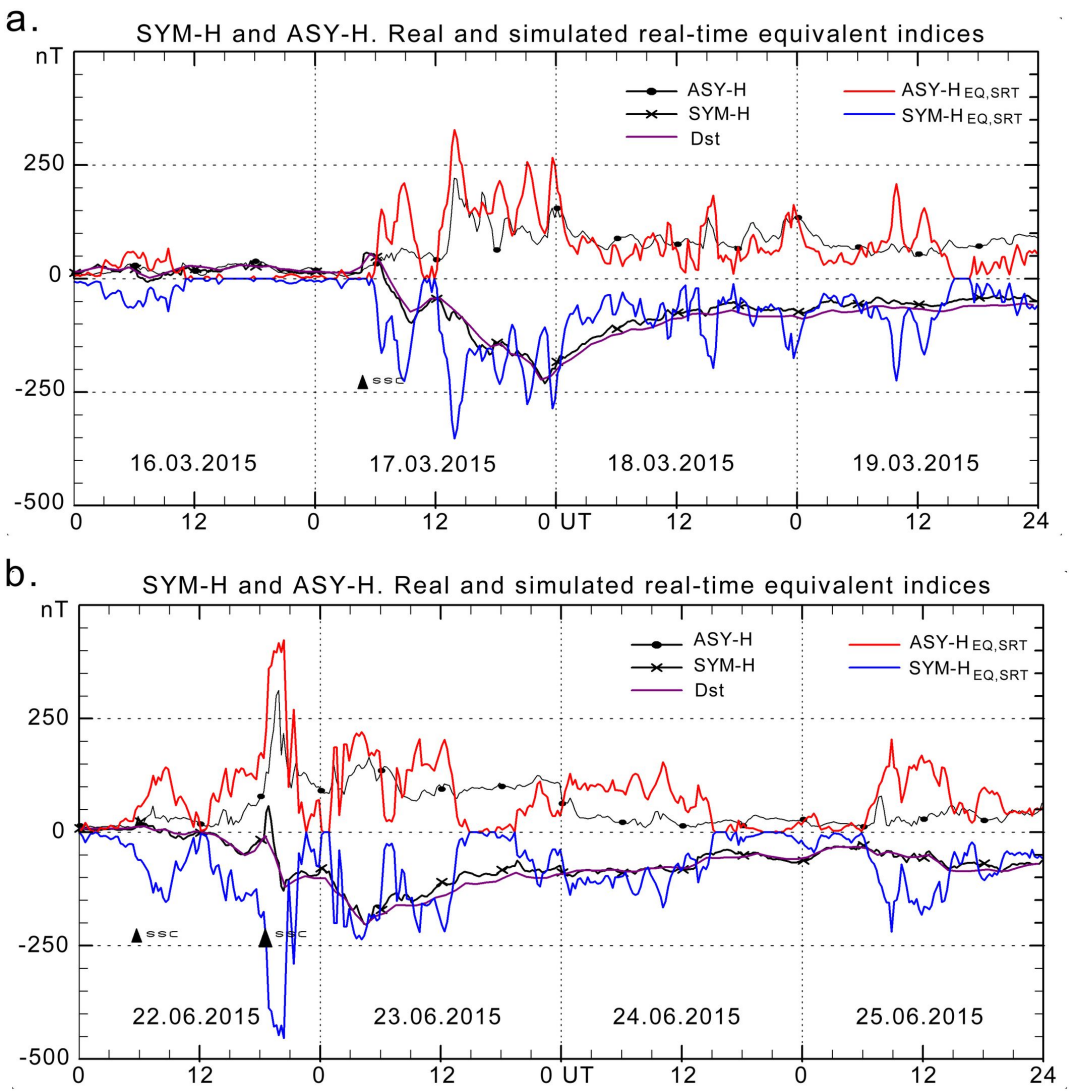
a.
SYM-H and ASY-H. Real and simulated real-time equivalent indices
nT
250
0
-250
-500
ASY-H
SYM-H
Dst
ASY-H EQ,SRT
SYM-H EQ,SRT
SSC
16.03.2015
17.03.2015
18.03.2015
19.03.2015
0
12
0
12
0 UT
12
0
12
24
b.
SYM-H and ASY-H. Real and simulated real-time equivalent indices
nT
250
0
-250
-500
ASY-H
SYM-H
Dst
ASY-H EQ,SRT
SYM-H EQ,SRT
SSC
SSC
22.06.2015
23.06.2015
24.06.2015
25.06.2015
0
12
0
12
0 UT
12
0
12
24

Figure 7.

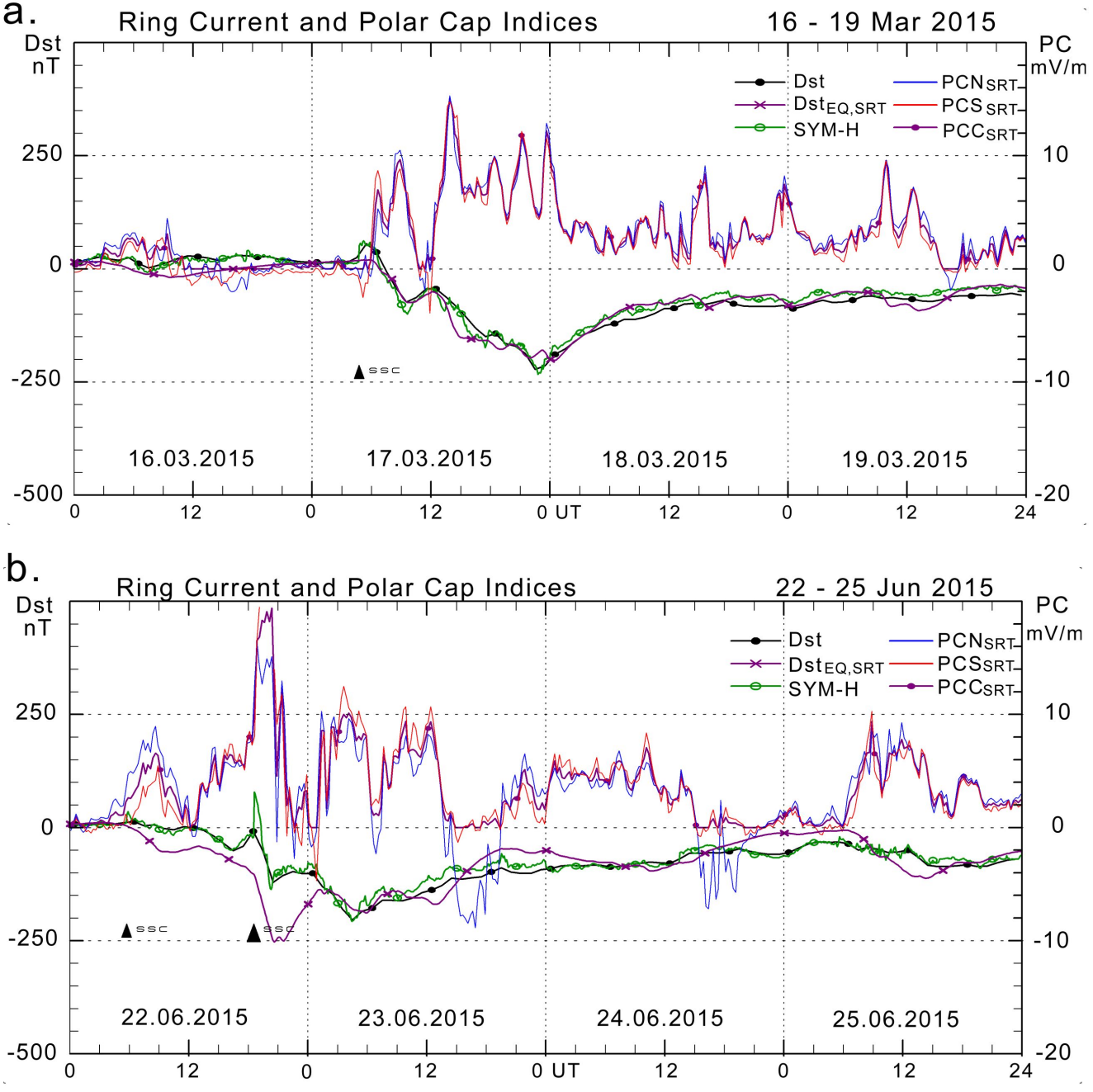
a.
Ring Current and Polar Cap Indices
16 - 19 Mar 2015
Dst
nT
PC
mV/m
Dst
Dst EQ,SRT
SYM-H
PCN SRT
PCS SRT
PCC SRT
250
0
-250
-500
10
0
-10
-20
SSC
16.03.2015
17.03.2015
18.03.2015
19.03.2015
0
12
0
12
0 UT
12
0
12
24
b.
Ring Current and Polar Cap Indices
22 - 25 Jun 2015
Dst
nT
PC
mV/m
Dst
Dst EQ,SRT
SYM-H
PCN SRT
PCS SRT
PCC SRT
250
0
-250
-500
10
0
-10
-20
SSC
SSC
22.06.2015
23.06.2015
24.06.2015
25.06.2015
0
12
0
12
0 UT
12
0
12
24

Figure 8.

Dst and Dst_{EQ}(simulated real-time) 1.1. - 31.12.2015

nT

Jan
0
-100

Feb
0
-100

Mar
0
-100

Apr
0
-100

May
0
-100

Jun
0
-100

Jul
0
-100

Aug
0
-100

Sep
0
-100

Oct
0
-100

Nov
0
-100

Dec
0
-100
-200

5 10 15 20 25 30

Figure A1.

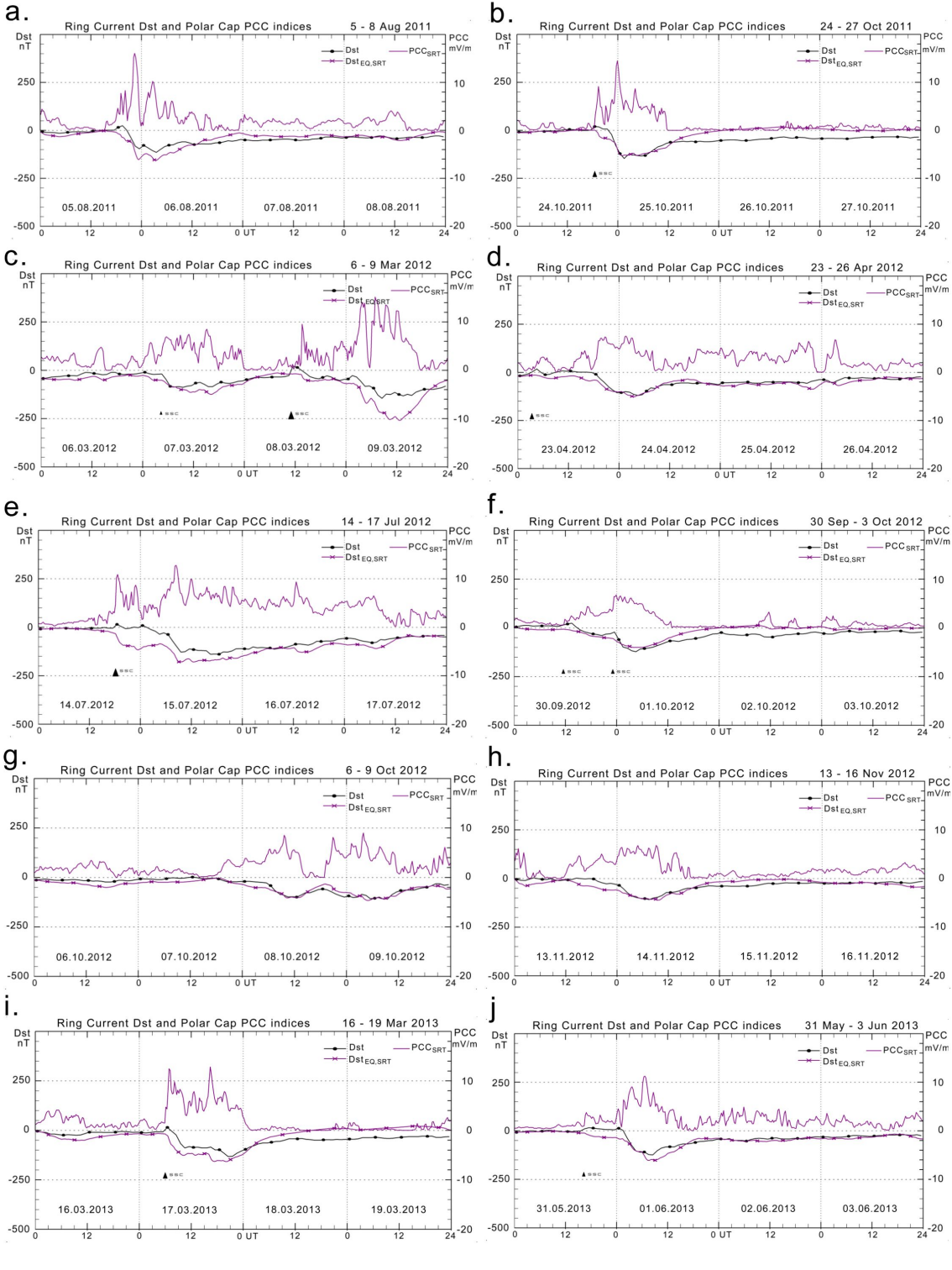
a.
Ring Current Dst and Polar Cap PCC indices
5 - 8 Aug 2011
b.
Ring Current Dst and Polar Cap PCC indices
24 - 27 Oct 2011
c.
Ring Current Dst and Polar Cap PCC indices
6 - 9 Mar 2012
d.
Ring Current Dst and Polar Cap PCC indices
23 - 26 Apr 2012
e.
Ring Current Dst and Polar Cap PCC indices
14 - 17 Jul 2012
f.
Ring Current Dst and Polar Cap PCC indices
30 Sep - 3 Oct 2012
g.
Ring Current Dst and Polar Cap PCC indices
6 - 9 Oct 2012
h.
Ring Current Dst and Polar Cap PCC indices
13 - 16 Nov 2012
i.
Ring Current Dst and Polar Cap PCC indices
16 - 19 Mar 2013
j.
Ring Current Dst and Polar Cap PCC indices
31 May - 3 Jun 2013
Dst nT
PCC mV/m
Dst
Dst EQ,SRT
PCC SRT
ssc
UT

Figure A2.

a.

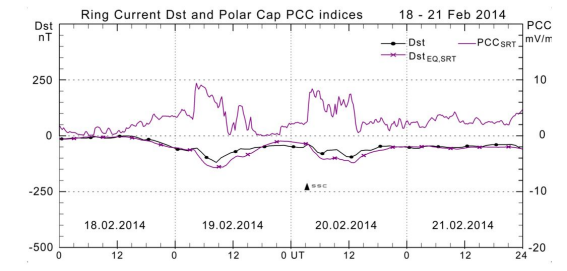
Ring Current Dst and Polar Cap PCC indices
18 - 21 Feb 2014
Dst nT
PCC mV/m
Dst
PCC SRT
Dst EQ,SRT
18.02.2014
19.02.2014
20.02.2014
21.02.2014
0 UT

b.

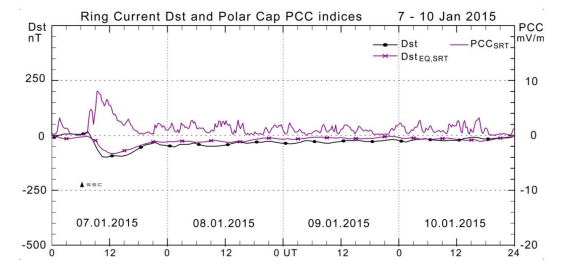
Ring Current Dst and Polar Cap PCC indices
7 - 10 Jan 2015
Dst nT
PCC mV/m
Dst
PCC SRT
Dst EQ,SRT
07.01.2015
08.01.2015
09.01.2015
10.01.2015
0 UT

c.

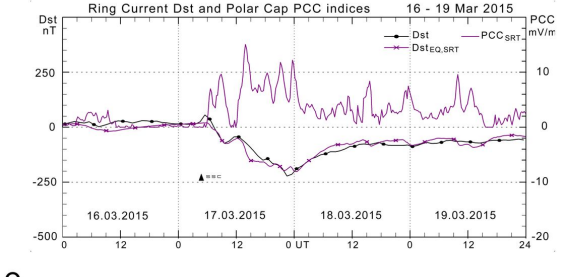
Ring Current Dst and Polar Cap PCC indices
16 - 19 Mar 2015
Dst nT
PCC mV/m
Dst
PCC SRT
Dst EQ,SRT
16.03.2015
17.03.2015
18.03.2015
19.03.2015
0 UT

d.

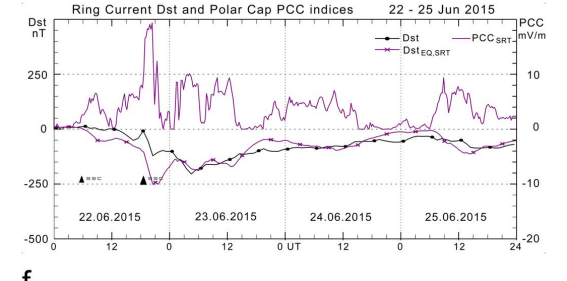
Ring Current Dst and Polar Cap PCC indices
22 - 25 Jun 2015
Dst nT
PCC mV/m
Dst
PCC SRT
Dst EQ,SRT
22.06.2015
23.06.2015
24.06.2015
25.06.2015
0 UT

e.

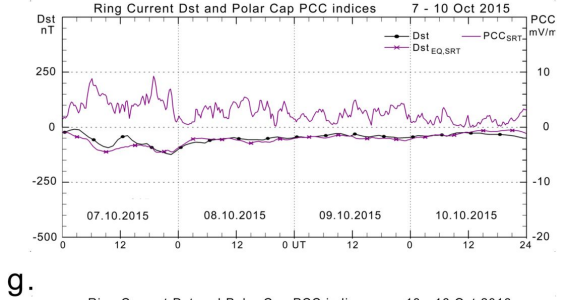
Ring Current Dst and Polar Cap PCC indices
7 - 10 Oct 2015
Dst nT
PCC mV/m
Dst
PCC SRT
Dst EQ,SRT
07.10.2015
08.10.2015
09.10.2015
10.10.2015
0 UT

f.

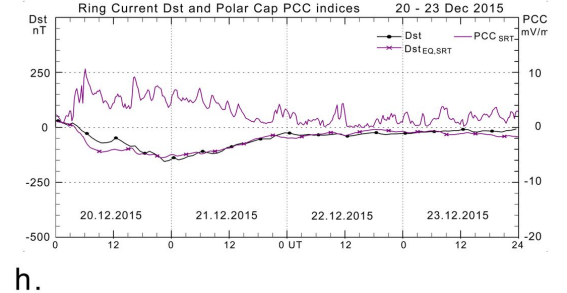
Ring Current Dst and Polar Cap PCC indices
20 - 23 Dec 2015
Dst nT
PCC mV/m
Dst
PCC SRT
Dst EQ,SRT
20.12.2015
21.12.2015
22.12.2015
23.12.2015
0 UT

g.

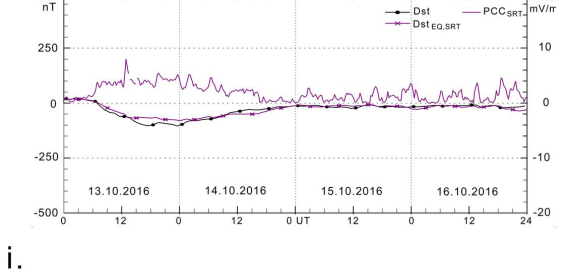
Ring Current Dst and Polar Cap PCC indices
13 - 16 Oct 2016
Dst nT
PCC mV/m
Dst
PCC SRT
Dst EQ,SRT
13.10.2016
14.10.2016
15.10.2016
16.10.2016
0 UT

h.

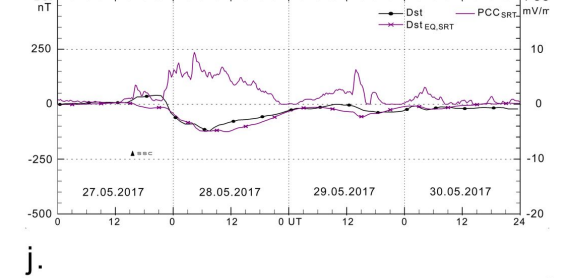
Ring Current Dst and Polar Cap PCC indices
27 - 30 May 2017
Dst nT
PCC mV/m
Dst
PCC SRT
Dst EQ,SRT
27.05.2017
28.05.2017
29.05.2017
30.05.2017
0 UT

i.

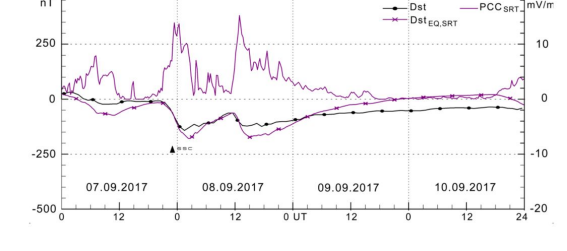
Ring Current Dst and Polar Cap PCC indices
7 - 10 Sep 2017
Dst nT
PCC mV/m
Dst
PCC SRT
Dst EQ,SRT
07.09.2017
08.09.2017
09.09.2017
10.09.2017
0 UT

j.

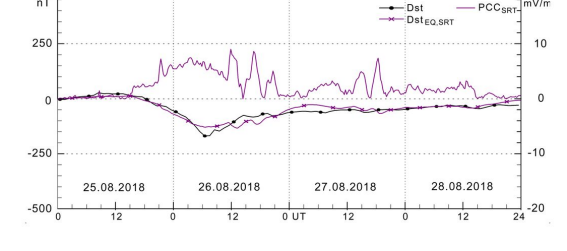
Ring Current Dst and Polar Cap PCC indices
25 - 28 Aug 2018
Dst nT
PCC mV/m
Dst
PCC SRT
Dst EQ,SRT
25.08.2018
26.08.2018
27.08.2018
28.08.2018
0 UT

Figure A3.

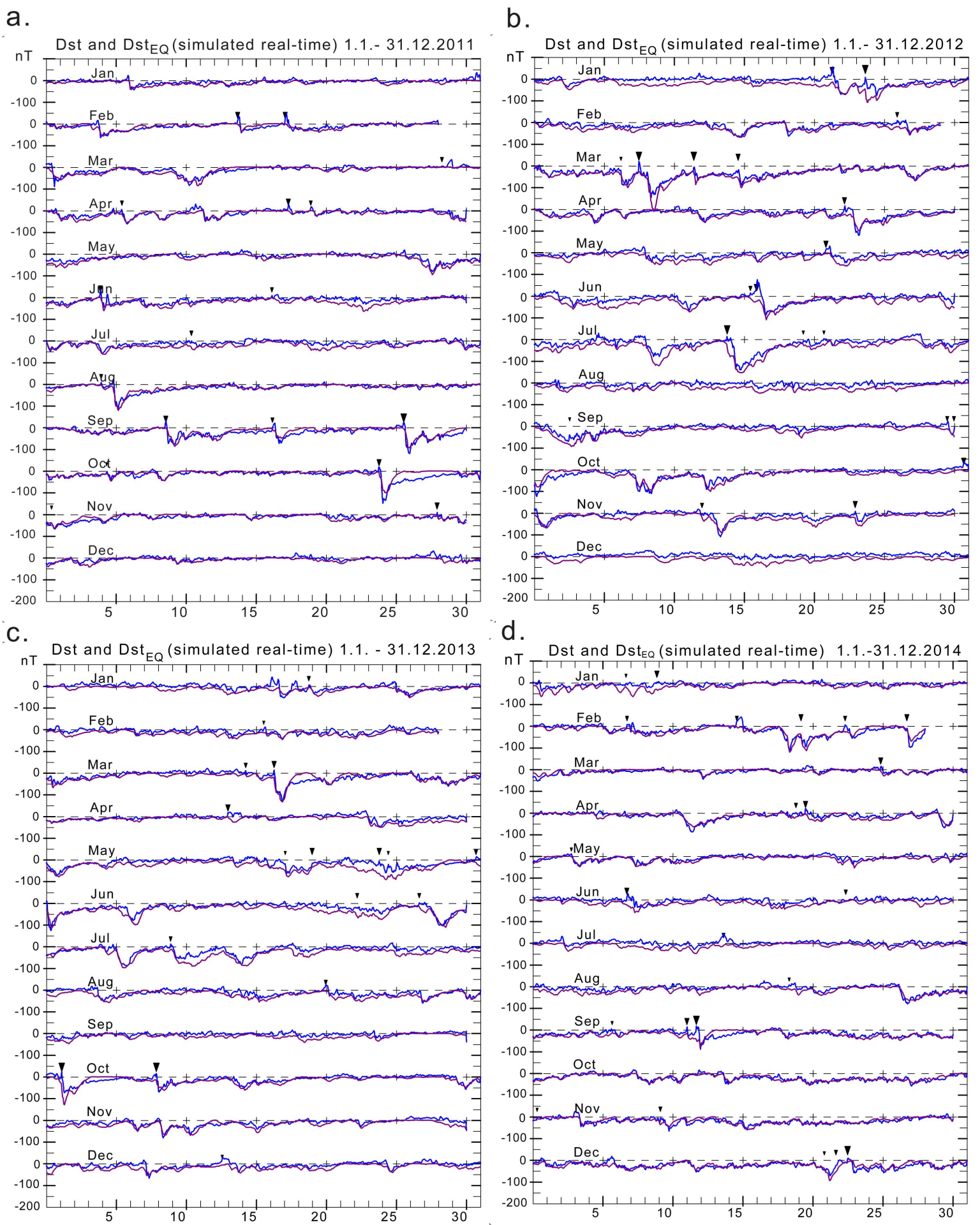
a.
Dst and Dst$_{EQ}$ (simulated real-time) 1.1.- 31.12.2011
b.
Dst and Dst$_{EQ}$ (simulated real-time) 1.1.- 31.12.2012
c.
Dst and Dst$_{EQ}$ (simulated real-time) 1.1. - 31.12.2013
d.
Dst and Dst$_{EQ}$ (simulated real-time) 1.1.-31.12.2014
nT
Jan
Feb
Mar
Apr
May
Jun
Jul
Aug
Sep
Oct
Nov
Dec
0
-100
-200
5
10
15
20
25
30

Figure A4.

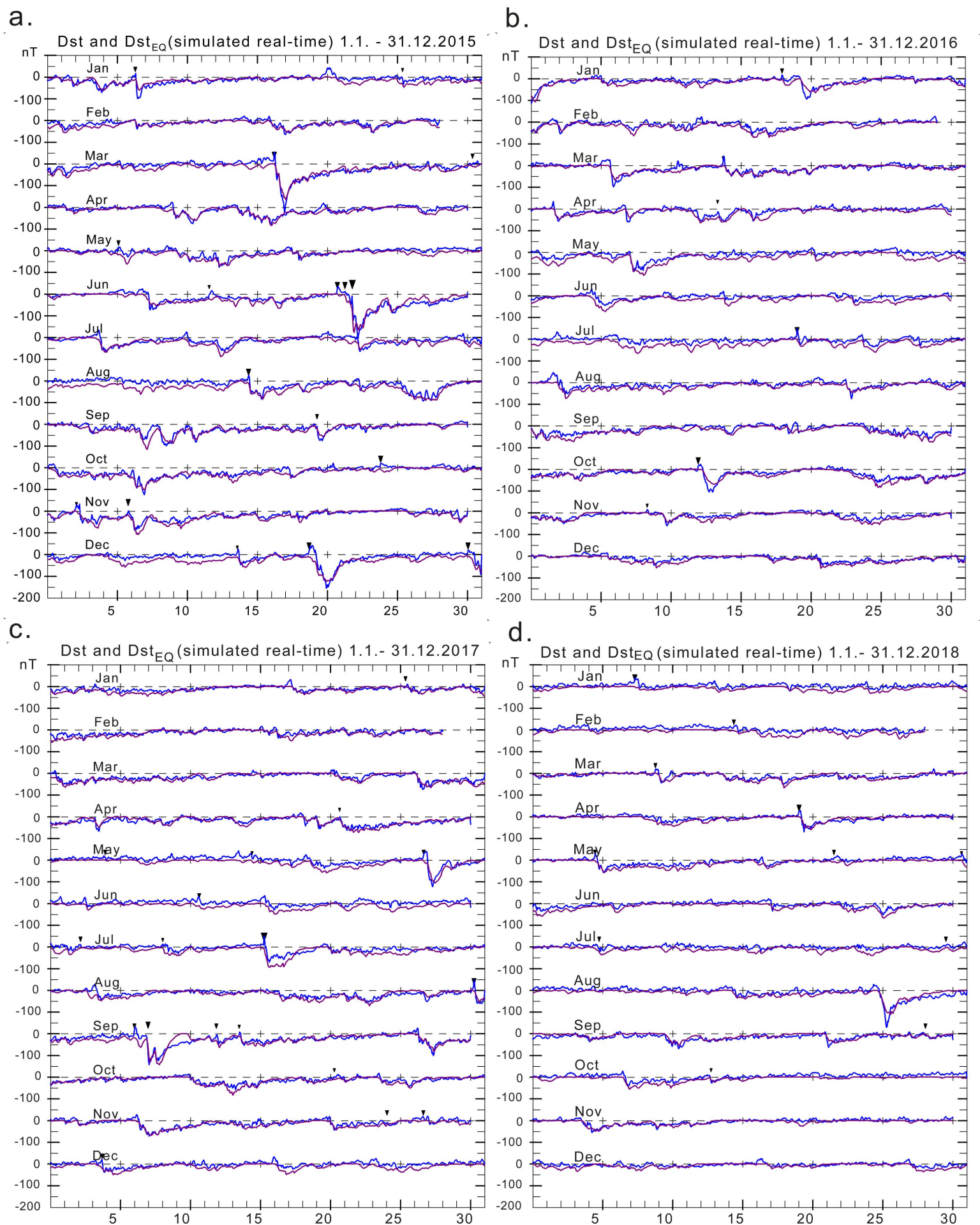
a.
Dst and Dst$_{EQ}$(simulated real-time) 1.1. - 31.12.2015
b.
Dst and Dst$_{EQ}$ (simulated real-time) 1.1.- 31.12.2016
c.
Dst and Dst$_{EQ}$ (simulated real-time) 1.1.- 31.12.2017
d.
Dst and Dst$_{EQ}$ (simulated real-time) 1.1.- 31.12.2018
nT
Jan
Feb
Mar
Apr
May
Jun
Jul
Aug
Sep
Oct
Nov
Dec
0
-100
-200
5
10
15
20
25
30

Epoch 2009-2018	PCCD	PCC	PCN	PCS	PCD
Post-Event	**0.753**	0.751	0.696	0.722	0.736
Real-Time	**0.749**	0.748	0.692	0.720	0.728

PCC version	No. samples	Mean ASY-H	Mean PCC	Mean Error	RMS error	Correlation
Post-Event	7349	38.5 nT	2.07 mV/m	5.9 nT	21.7 nT	0.752
Real-Time	7350	38.5 nT	2.46 mV/m	1.8 nT	21.6 nT	0.737

PCC version	0 min.	60 min	120 min	180 min	240 min
Post-event	0.531	0.619	0.632	0.636	0.643
Real-time	0.530	0.614	0.625	0.628	0.632

Evnt	Date	Dst_{MIN}	$SymH_{MIN}$	$T_{SYMHMIN}$	$Dst_{EQ,MIN}$	Corr.	Avr.dif.	Abs.dif.	Rms.dif.	PCC_{MAX}	T_{PCCMAX}
No.	dd.mm.yyyy	nT	nT	min[(2)]	nT	coeff.	nT[(1)]	nT[(1)]	nT[(1)]	mV/m	min[(2)]
1	05.08.2011	-115	-126	1620	-157	0.772	-0.6	18.3	22.7	17.98	1335
2	24.10.2011	-147	-160	1500	-132	0.748	24.7	31.6	37.1	15.07	1430
3	06.03.2011	-145	-149	4800	-259	0.903	-26.6	29.6	42.0	16.77	4735
4	23.04.2012	-120	-125	1675	-127	0.877	-10.3	14.1	17.6	7.72	1525
5	14.07.2012	-139	-122	2400	-179	0.850	-29.2	29.6	39.8	13.54	1930
6	30.09.2012	-122	-138	1675	-100	0.762	15.0	22.9	26.0	6.91	1430
7	06.10.2012	-109	-116	4800	-116	0.911	-7.6	14.3	16.6	9.59	1445
8	13.11.2012	-108	-117	1855	-111	0.780	-2.5	15.2	18.4	6.85	1725
9	16.03.2013	-132	-131	2640	-158	0.730	7.9	32.3	36.1	12.89	2415
10	31.05.2013	-124	-135	1905	-152	0.887	-10.1	12.8	18.8	11.60	1840
11	18.02.2014	-119	-125	1920	-142	0.915	-7.9	12.5	18.0	9.60	1705
12	07.01.2015	-100	-135	650	-83	0.820	9.5	13.5	16.1	8.65	570
13	16.03.2015	-222	-233	2760	-202	0.960	-2.4	15.7	18.5	16.08	2270
14	22.06.2015	-204	-207	1680	-253	0.775	-4.8	26.8	37.2	20.19	1215
15	07.10.2015	-124	-124	1315	-114	0.832	-5.1	11.4	15.1	9.66	1130
16	20.12.2015	-155	-169	1320	-138	0.935	-4.6	11.8	15.9	11.04	360
17	13.10.2016	-104	-114	1380	-79	0.920	2.4	9.7	12.8	8.27	770
18	27.05.2017	-122	-141	1860	-125	0.864	-7.6	16.3	21.2	9.66	1700
19	07.09.2017	-142	-144	1500	-179	0.765	8.9	35.2	39.6	15.66	2210
20	25.08.2018	-169	-205	1800	-134	0.923	1.9	11.7	16.4	9.18	2150
Avr		-136	-133	2053[(3)]	-147	0.821	-2.5	19.3	24.3	11.85	1695[(3)]

Correlation	PCC	PCN	PCS	PCA[1)]	PCW[2)]	PCU[3)]
E_M	**0.764**	0.714	0.727	0.720	0.732	0.707
Kp	**0.820**	0.756	0.764	0.791	0.799	0.729
ASY-H[4)]	**0.743**	0.702	0.679	0.716	0.700	0.683